Measurement Report: Characterization of Aerosol Hygroscopicity over Southeast Asia during the NASA CAMP²Ex Campaign

Genevieve Rose Lorenzo[1,2], Luke D. Ziemba[3], Avelino F. Arellano[1], Mary C. Barth[4], Ewan C. Crosbie[3,5], Joshua P. DiGangi[3], Glenn S. Diskin[3], Richard Ferrare[3], Miguel Ricardo A. Hilario[1], Michael A. Shook[3], Simone Tilmes[4], Jian Wang[6], Qian Xiao[6], Jun Zhang[4], and Armin Sorooshian[1,7]

[1]Department of Hydrology and Atmospheric Sciences, University of Arizona, Tucson, Arizona, 85721, USA
[2]Manila Observatory, Quezon City, 1108, Philippines
[3]NASA Langley Research Center, Hampton, Virginia, 23681 USA
[4]Atmospheric Chemistry Observations & Modeling Laboratory, NSF National Center for Atmospheric Research, Boulder, Colorado, 80301, USA
[5]Analytical Mechanics Associates, Inc, Hampton, Virginia, 23666 USA
[6]Department of Energy, Environmental & Chemical Engineering, Washington University in St Louis, St. Louis, Missouri, 63130, USA
[7]Department of Chemical and Environmental Engineering, University of Arizona, Tucson, Arizona, 85721, USA

Correspondence to: armin@arizona.edu

Abstract. This study characterizes the spatial and vertical nature of aerosol hygroscopicity in Southeast Asia and relates it to aerosol composition and sources. Aerosol hygroscopicity via the light scattering hygroscopic growth factor, f(RH), is calculated from the amplification of PM_5 aerosol ($D_p < 5$ μm) scattering measurements from < 40% to 82% relative humidity during the Cloud, Aerosol, and Monsoon Processes Philippines Experiment (CAMP²Ex) between August to October 2019 over the northwest tropical Pacific. Median f(RH) is low (1.26 with lower to upper quartiles of 1.05 to 1.43) like polluted environments, due to the dominance of the mixture of organic carbon and elemental carbon. The f(RH) is lowest due to smoke from the Maritime Continent (MC) during its peak biomass burning season, coincident with high carbon monoxide concentrations (> 0.25 ppm) and pronounced levels of accumulation mode particles and organic mass fractions. The highest f(RH) values are linked to coarser particles from the West Pacific and aged biomass burning particles in the region farthest away from the MC, where f(RH) values are lower than typical polluted marine environments. Convective transport and associated cloud processing in these regions decrease and increase hygroscopicity aloft in cases with transported air masses exhibiting increased organic and sulfate mass fractions, respectively. An evaluation of a global chemical transport model (CAM-chem) for cases of vertical transport showed the underrepresentation of organics resulting in overestimated modeled aerosol hygroscopicity. These findings on aerosol hygroscopicity can help to improve aerosol representation in models and the understanding of cloud formation.

1. Introduction

Aerosol particles affect climate and visibility through the direct and indirect extinction of solar radiation via absorption and scattering of light and through cloud formation, respectively. Aerosol hygroscopicity compounds aerosol effects on Earth's radiation budget (Zhao et al., 2018; Malm and Day, 2001), secondary aerosol formation and cloud formation (Köhler, 1936), and health (Dockery, 2001). Neglecting the effect of moisture on aerosol growth leads to incorrect estimation of the cooling at Earth's surface due to aerosol particles (Garland et al., 2007). For instance, a decrease in light extinction over the southeast U.S. was linked to reduced aerosol water uptake, coincident with decreases in the sulfate/organic ratio (Attwood et al., 2014). Particle aging/coating can cause underestimation of both aerosol hygroscopicity in the sub-saturated regime (Wang et al., 2018) and cloud condensation nuclei (CCN) activity in the supersaturated regime for aged particles in China by ~22% (Zhang et al., 2017). Remote sensing of aerosol optical properties is also affected by aerosol water content (Ferrare et al., 1998; Ferrare et al., 2023). Therefore, accurate aerosol hygroscopicity values are critical for remote sensing and satellite observation of aerosol particles (Ziemba et al., 2013; van Diedenhoven et al., 2022).

Aerosol hygroscopicity is described by physical quantities such as the diameter growth factor, g(RH), and light scattering hygroscopic growth factor, f(RH). The g(RH) parameter relates the wet particle diameter of the aerosol at a high relative humidity to the dry diameter of the aerosol at low relative humidity, while f(RH) relates total scattering due to the aerosol at high relative humidity (80%) to that at low relative humidity (<40%) (Waggoner et al., 1983; Hegg et al., 1993). Light scattering increases with relative humidity for most particles and is correlated to chemical composition and size (Baynard et al., 2006; Swietlicki et al., 2008) of particulate matter (Covert et al., 1972; Brock et al., 2016a).

Direct measurement of aerosol hygroscopicity, however, is difficult and is also not well-represented in climate models (Chen et al., 2014). The hygroscopicity parameter kappa, κ, is a single parameter that was developed to represent water uptake in models. It determines the volume (or mass or moles, with appropriate unit conversions) of water that is associated with a unit volume of a dry aerosol particle (Petters and Kreidenweis, 2007). A simple and commonly used water uptake model for calculating kappa is based on the Zdanovskii, Stokes, and Robinson (ZSR) treatment for water soluble organic-inorganic mixed aerosol particles (Stokes and Robinson, 1966) where it is assumed that there are no interactions between the organic and inorganic species. In the ZSR model, water uptake of the individual non-interacting components can be summed up linearly to represent the total water uptake of the mixed aerosol. The interaction of organics and inorganics, however, along with the aging-specific density of organics is thought to influence hygroscopicity and affect both the ZSR calculation (Fan et al., 2020) and aerosol particle growth factor via changes in molecular structure, molecular weight, functionality, and/or other properties (Swietlicki et al., 2008).

Table 1: Hygroscopicity values of various aerosol types based on selected summary studies for measured g(RH) (Swietlicki et al., 2008) and f(RH) (Burgos et al., 2019; Titos et al., 2021) and modeled κ (Pringle et al., 2010).

Aerosol Type	g(RH=90%) (10 - 500 nm)	f(RH=85%/RH=40%) (< 1000 nm)	κ (5 - 500 nm)
Clean Marine	1.62 - 2.14	2.10 - 2.30	0.92
Polluted Marine	1.00 - 1.76	1.60 - 2.20	0.59
Background Continental	1.00 - 1.60	1.29 - 1.40	0.15 - 0.17
Urban Continental	1.00 - 1.68	1.38 - 2.10	0.21 - 0.36
Aged Biomass	1.15 - 1.30	1.02 - 2.10*	< 0.1
New Particle Formation	1.04 - 1.40	-	-
Free Troposphere	1.21 - 1.47	-	site specific
Arctic	1.19 - 1.44	2.70	~0.4

*Gomez et al., 2018 (f(RH=85%/RH=25%))

68 Observed and simulated aerosol hygroscopicity using aforementioned parameters are greater (Table 1) in clean marine
69 air masses compared to air masses over land, near terrestrial biogenic sources which are secondary organics precursors,
70 and under polluted conditions (Swietlicki et al., 2008; Duplissy et al., 2011; Petters and Kreidenweis, 2007; Burgos
71 et al., 2019; Titos et al., 2021). In marine areas, hygroscopicity typically decreases with altitude with decreasing
72 inorganic fractions (Pringle et al., 2010). Cloud processing over marine areas has been observed to increase the
73 oxidation of organic aerosols (Che et al., 2022; Dadashazar et al., 2022) and hygroscopicity in general (Crumeyrolle
74 et al., 2008). Continental aerosol particles have smaller diameters and are usually less hygroscopic due to more
75 organic-rich aerosol particles (κ = 0 - 0.1 from Table S1) and pure elemental carbon particles (EC, κ = 0 - 0.035 from
76 Table S1) (Wang et al., 2014; Kreidenweis and Asa-Awuku, 2014). Organics are generally less hygroscopic than
77 inorganics (κ = 0.56 – 1.24 from Table S1), and their hygroscopicity is affected by oxidation level (e.g., O:C ratio),
78 oxidation state, and solubility (Brock et al., 2016a; Wu et al., 2016; Thalman et al., 2017). Aging has also been found
79 to increase aerosol hygroscopicity through the oxidation of secondary organic aerosols and organic aerosol interactions
80 with inorganics (Engelhart et al., 2008; Liu et al., 2014; Saxena et al., 1995).

81 Although aerosol studies in the rapidly developing Southeast Asia (SEA) region are increasing, few are focused on
82 the nature of aerosol particles and their interactions with water vapor and clouds (Tsay et al., 2013; Ross et al., 2018;
83 Reid et al., 2023). There has been no comprehensive study of aerosol hygroscopicity in and around the Philippines in
84 Southeast Asia. Understanding the interactions between aerosols and the complex geographic, meteorological, and
85 hydrological environment in Southeast Asia remains challenging due to a still growing observational database,
86 prevalence of clouds interfering with remote sensing, and limited modeling studies (Tsay et al., 2013; Lee et al., 2018;
87 Chen et al., 2020; Hong and Di Girolamo, 2020; Amnuaylojaroen, 2023). This, along with increased local and
88 transported emissions and prevalent moisture-rich conditions in the region, altogether motivate the need to understand
89 aerosol hygroscopicity and associated impacts on radiative transfer and on climate (Brock et al., 2016a; Ziemba et al.,
90 2013). How freshly emitted nearly hydrophobic particles transform into hygroscopic aerosol particles (Swietlicki et

al., 2008), for example, is an understudied topic in Southeast Asia where there are significant sources of particles with low hygroscopicity (Reid et al., 2023). Understanding aerosol hygroscopicity will also help in the need to improve remote sensing measurements in the region, which is affected by overlapping high and low level clouds (Burgos et al., 2019; Hong and Di Girolamo, 2020).

Predicting aerosol hygroscopicity, especially at higher relative humidity (RH), is especially difficult due to optical instruments underestimating particle light scattering at high RH and mechanisms other than hygroscopicity impacting particle growth (Gasparini et al., 2006; Mochida et al., 2006). This is important because atmospheric water content is high in Southeast Asia. For example, the hygroscopicity of secondarily formed organics (via gas-to-particle conversion) is found to be dependent on oxidation state for high RH (Shi et al., 2022). Southeast Asia has elevated levels of organics, inorganics, and elemental carbon (Cruz et al., 2019; AzadiAghdam et al., 2019; Oanh et al., 2006), allowing for an opportunity to see how hygroscopicity responds to a range of relative values of each of these elevated components. Therefore, relating aerosol particle composition to hygroscopicity, for closure (Xu et al., 2020), is particularly significant there.

Aerosol hygroscopicity is a crucial factor in the understanding and modeling of aerosol-cloud interactions, because of the role hygroscopicity plays in cloud drop activation. The NASA Cloud, Aerosol, and Monsoon Processes Philippines Experiment (CAMP^{2}Ex) was designed to understand the role of aerosol particles in cloud formation and in regulating solar radiation during the southwest monsoon (Reid et al., 2023). CAMP^{2}Ex occurred between August and October 2019 over the Philippines and neighboring areas. The campaign provides an aircraft dataset with measurements focused on aerosol and cloud properties, which affords a valuable opportunity to evaluate models with these measurements for shallow to moderate convection, which is one of the biggest challenges for regional and global-scale atmosphere models to represent because these clouds are much smaller than the model grid spacing.

Global atmospheric model evaluation of aerosol extinction for the CAMP^{2}Ex region suggests that biomass burning aerosol hygroscopicity is over-estimated by global atmosphere models, with both the model size representation of the aerosol particles and the size discrepancy between model and observations contributing to this (Collow et al., 2022; Edwards et al., 2022). The findings from Collow et al. (2022) and Edwards et al. (2022) bring up the need for a more thorough understanding of the components of biomass burning aerosols in the region that affect observed and modeled hygroscopicity. The overestimation of hygroscopicity due to biomass burning can affect the representation of clouds in the region. Clouds, especially shallow cumulus clouds, like those in the tropical West Pacific (which the CAMP^{2}Ex region is part of) have been underestimated by models due to the lack of observational data to improve convective parameterizations (Chandra et al., 2015). Part of the challenge in modeling aerosol-cloud interactions is the ability to both have a high-resolution representation, at the scale of the shallow convection, in a large enough domain, which is important for understanding climatic effects to properly account for the bulk behavior of cloud fields (Spill et al., 2019). This could be addressed by evolving modeling infrastructures, with higher resolution schemes ranging from regional to convective scale within a larger domain (Pfister et al., 2020; Radtke et al., 2021).

125   Knowledge gaps identified above are addressed in this study using the CAMP²Ex dataset. To our knowledge, this is

126   the first time this dataset has been explored extensively to characterize aerosol hygroscopicity properties in the region.

127   The goals of this proposed study are to (i) characterize the spatial distribution of aerosol hygroscopicity in Southeast

128   Asia during the CAMP²Ex airborne mission, (ii) relate aerosol hygroscopicity and composition, (iii) identify emission

129   events that impact aerosol hygroscopic growth, and (iv) evaluate a global chemical transport model with regional

130   refinement for aerosol vertical transport.

131

132   **2. Methods**

133   **2.1 CAMP²Ex Field Campaign**

134   CAMP²Ex included 19 research flights with a NASA P3 from 24 August to 5 October 2019. Twelve of these flights

135   were associated with the southwest monsoon (SWM) followed by a flow reversal with seven flights conducted during

136   the northeast monsoon (NEM) (Reid et al., 2023). As summarized by Reid et al. (2023), the combination of airborne

137   and ship-based measurements helps to characterize interactions between various aerosol particle sources (e.g., biomass

138   burning, industrial, natural) and small to congestus convection. Below we note the P3 instruments most relevant to

139   this study.

140   **2.2 Observations and Derived Quantities**

141   **2.2.1 P3 Instrumentation**

142   As summarized in Table 2, data are used from a variety of aerosol particle and trace gas instrumentation. The aerosol

143   particle scattering and absorption instruments measure the optical properties of bulk aerosol particles (PM_5): < 5 μm

144   dry diameter (McNaughton et al., 2007). Aerosol composition and size data for submicrometer particles were

145   considered when they were collected using a forward-facing shrouded isokinetic inlet. Non-refractory species in the

146   submicrometer range studied using an aerosol mass spectrometer (AMS) included sulfate, nitrate, ammonium,

147   organics, and chloride. We also use the ratio of the mass spectral marker m/z 44 marker relative to total organic mass,

148   f_{44}, as a possible indicator of air mass age. Submicrometer refractory species of black carbon (also referred to as

149   elemental carbon) from a single particle poot photometer (SP2) were also included in the study. Bulk water-soluble

150   aerosol particles were collected using a particle-into-liquid sampler (PILS) and were analyzed using ion

151   chromatography; species quantified included oxalate, NH_4^+, dimethylamine (DMA), K^+, SO_4^{2-}, Ca^{2+}, Na^+, Mg^{2+}, Cl^-,

152   NO_3^-, Br^-, and NO^-. Cloud-free conditions are identified to ensure the highest quality aerosol data using a cloud flag

153   product based on measurements from the fast cloud droplet probe (FCDP) and two-dimensional stereo probe (2D-S).

154   Aerosol particle composition data are considered for those cases when the total aerosol non-refractory particle mass

155   was greater than 0.4 μg sm^{-3}.

156   **Table 2: Summary of instrument data used in this work.**

Parameter	Instrument	Time Resolution	Uncertainty	Sampled Aerosol Particle Size	Reference
Latitude, Longitude, and Altitude	Northrop Grumman Litton 251 EGI	1 s	~5 m spherical error probable; 0.01°	N/A	Reid et al., 2023
Dry (RH < 40%) and humidified (RH = 80%)) light scattering coefficient (λ = 450, 550, 700 nm)	Parallel humidified TSI 3563 Nephelometers	1 s	30%	< 5μm diameter	Ziemba et al., 2013; McNaughton et al., 2007
Dry (RH < 40%) light absorption coefficient (λ = 470, 532, 660 nm)	Radiance Research 3 Particle Soot Absorption Photometer (PSAP)	1 s	15%	< 5μm diameter	Mason et al., 2018; McNaughton et al., 2007
Non-refractory aerosol (Organics, SO_4, NO_3, NH_4, Cl) mass concentration	Aerodyne High-Resolution Time-of-Flight Mass Spectrometer (AMS)	25 s	LLOD (μg sm^{-3}): Organics, 0.169; SO_4, 0.039; NO_3, 0.035; NH_4, 0.169; Cl, 0.036; Uncertainty: 50%	approximate relevant size range is 60-600 nm vac. aero. diameter	DeCarlo et al., 2008
Water-soluble mass concentration	Particle-into-liquid sampler (PILS) followed by offline ion chromatography analysis	238 s	30%	< 5μm diameter	Sorooshian et al., 2006 Crosbie et al., 2020
Refractory black carbon (BC) mass concentration	Single Particle Soot Photometer (DMT SP2)	1 s	10%	100 - 700 nm diameter	Schwarz et al., 2006
CO concentration	Picarro G2401-m	1 s	5 ppb	N/A	DiGangi et al., 2021
Volume and number concentration of particles	TSI Laser Aerosol Spectrometer (LAS) Model 3340	1 s	20%	0.1 - 5 μm optical diameter	Moore et al., 2021
Volume size distribution	Fast integrated mobility spectrometer (FIMS)	1 s	Concentration: 15%; Size: 3%	10 – 500 nm mobility diameter	Kulkarni and Wang, 2006;

					Wang et al., 2017; 2018
Cloud particles (data used for cloud screening)	SPEC-Hawkeye FCDP	1 s	50%	2 – 50 μm diameter	Knollenberg 1981, Lawson et al. 2017; Woods et al. 2018
Cloud particles (data used for cloud screening)	SPEC-Hawkeye 2D-S	1 s	20%	10 μm – 3 mm diameter	Lawson et al. 2006a, Woods et al. 2018

157

158 **2.2.2 Aerosol Hygroscopicity, f(RH), and Other Aerosol Optical Properties**

159 Aerosol hygroscopicity is reported using the parameter f(RH), which is unitless and is the amplification factor in

160 scattering due to a change in RH. The f(RH) parameter is calculated from the empirically derived exponential fit

161 coefficient gamma (γ) (Ziemba et al., 2013). The gamma parameter is based on parallel nephelometer measurements

162 of scattering at 550 nm at two different relative humidity levels: dry ($< 40\%$: RH_{dry}) and humidified (controlled to 82

163 $\pm 10\%$: RH_{wet}). Gamma (Eq. 1) was calculated for times when the dry (SC_{dry}) and humidified (SC_{wet}) scattering

164 coefficients (Table 2) are greater than or equal to 5 Mm^{-1}. The f(RH) (Eq. 2) was then derived from γ (Hänel, 1976).

165

166
$$\gamma = \frac{\ln\frac{SC_{wet}}{SC_{dry}}}{\ln\frac{100 - RH_{dry}}{100 - RH_{wet}}} \qquad (1)$$

167
$$f(RH) = \left(\frac{100 - RH_{wet}}{100 - RH_{dry}}\right)^{-\gamma} \qquad (2)$$

168 Each nephelometer was calibrated with pure CO_2 prior to the campaign and zero checks were performed periodically

169 during the flights to prevent baseline drift. Hydrophilic polystyrene latex (PSL) aerosol were also introduced

170 periodically in-flight to ensure the nephelometers were consistent. All nephelometer scattering coefficient

171 measurements were corrected for truncation errors using a documented method (Anderson and Ogren, 1998). System

172 response was verified in flight by introducing hydrophobic PSL spheres into the sample stream to ensure an f(RH)

173 value of 1.0 is observed. Relative humidity measurements for the calculation of f(RH) were calibrated in the laboratory

174 using nebulized monodisperse 200 nm ammonium sulfate to ensure deliquescence at ~80% RH and at the typical

175 measurement flow rates (i.e. 10 L min^{-1}) (Brooks et al., 2002). The RH was slowly ramped up from ~60% – 90% and

176 the apparent deliquescence RH was calculated based on the sharp increase in scattering in the humidogram. The offset

177 between the calculated RH and the deliquescence RH for ammonium sulfate (i.e., ~79.5%) was applied to the data

178 post-processing. Calibration at ~80% RH increases the confidence in the humidified nephelometer data accuracy.

179 Non-linearities can occur at low RH measurements and add to uncertainties, but the f(RH) calculation is much less

180 sensitive at the dry end of the spectrum. Internal RH sensors were used because their placement is most relevant to

181   the sampling condition inside the nephelometer. Note that sampling efficiency decreases for supermicrometer

182   diameter particles with increasing size up to the 5-µm inlet cutoff, due to losses in transport tubing and in the

183   drying/humidification control system. Thus, derived f(RH) is applicable to accumulation-mode particles and is

184   partially sensitive to coarse-mode particles from 1-5 µm diameter.

185

186   Single scattering albedo (SSA) was calculated when both the scattering and absorption coefficients (smoothed with

187   30 s running average) were greater than 2 Mm^{-1}. The Ångström exponent (AE) was calculated using the smoothed 30

188   s running average of the scattering and absorption coefficients. The scattering Ångström exponent (SAE, 450-700

189   nm) was computed when the scattering coefficient was greater than 2 Mm^{-1} based on Ziemba et al. (2013) and the

190   absorption Ångström exponent (AAE, 470-660 nm) was computed when the absorption coefficient was greater than

191   2 Mm^{-1} to try to minimize noise issues (Mason et al., 2018). Absorption measurements were corrected for a variety of

192   errors using the method from Virkkula (Virkkula, 2010). The PSAP filters were changed before transmission dropped

193   below 70%. This standard practice minimizes non-linearity effects due to filter loading.

194

195   **2.2.3 Sea Salt**

196   Bulk sea salt mass concentration was calculated using summed PILS concentrations of Na^+, Cl^-, and Mg^{2+} along with

197   the respective concentrations of the mass concentrations of K^+, Ca^{2+} and SO_4^{2-} in sea salt (0.037, 0.04 and 0.25,

198   respectively, by mass) (Crosbie et al., 2022).

199

200   **2.2.4 Aerosol Particle Classification**

201   Aerosol particle optical data were grouped depending on their AAE and SAE (Section 2.2.2) values and based on the

202   method of Cazorla et al. (2013), which used sun photometer measurements to arrive at the following classifications

203   as part of evaluating aircraft data over California, USA: coated large particles, dust and elemental carbon mix, dust

204   dominated, organic carbon and dust mix, organic carbon dominated, elemental carbon and organic carbon mix, mixed,

205   and elemental carbon dominated. This method has been used for cases when chemical composition is not available

206   (Höpner et al., 2019), and can be useful because the composition data from the AMS is limited to submicrometer

207   particles (0.06 to 0.6 µm vacuum aerodynamic diameter) while the f(RH) includes relatively larger particles (< 5 µm

208   dry diameter).

209

210   **2.2.5 Effective Particle Density**

211   Following Shingler et al. (Shingler et al., 2016b), effective particle density was calculated by dividing the sum of the

212   30 s total mass concentration from the AMS species (organics, SO_4^{2-}, NO_3^-, NH_4^+, and Cl^-) and 30 s averaged black

213   carbon from SP2 by the 30 s averaged integrated (for particles with diameter from 0.1 to 1 µm) volume concentration

214   from the LAS (Table 2).

215

216   **2.3 Modeling**

217

2.3.1 Trajectory Analysis

This work leverages trajectory results explained in detail by Hilario et al. (2021) using the National Oceanic and Atmospheric Administration (NOAA) Hybrid Single Particle Lagrangian Integrated Trajectory Model (HYSPLIT) (Stein et al., 2015; Rolph et al., 2017). Five-day HYSPLIT back trajectories from specific CAMP²Ex flight locations were associated with air masses undergoing long-range transport from either the Maritime Continent (MC), East Asia (EA), peninsular Southeast Asia (PSEA), or the West Pacific (WP) when they were within the regions at altitudes below 2 km for more than 6 h. The back trajectories were generated based on 1-minute resolution aircraft locations and 0.25° x 0.25° resolution NOAA Global Forecasting System (GFS) archived meteorological data. The source regions are approximately within the following lowest and highest latitude and longitude values, respectively: MC (-9.5° - 6.5° and 95° - 119°), EA (22° - 47° and 105° - 121.5°), PSEA (10° - 20° and 98° - 106 °), and WP (3°-25° and 120.5°-122.5°). The classification "Other" was used for back trajectories that either passed by the regions but at elevations above the boundary layer (defined as 2 km), came from sources farther away than the four listed above, were more localized to the Philippines, had too few sample counts, or were from stagnant air (Hilario et al., 2021).

2.3.2 CAM-chem Model Configuration

The Community Atmosphere Model with comprehensive tropospheric and stratospheric chemistry CAM-chem is used here as the atmospheric component of the Community Earth System Model (CESM2). CAM-chem includes the modal aerosol model (MAM4) (Liu et al., 2016) and results were evaluated with the CAMP²Ex AMS composition and f(RH) observations for two case studies. Two CAM-chem simulations with different horizontal resolutions were performed using the spectral element grid mesh and dynamical core. The grid mesh resolution for one simulation was uniform with ~111 km (labeled ne30). The other simulation employed regional refinement over East Asia with grid spacing ~27 km (labeled MUSICA) in the regionally refined region and ~111 km elsewhere across the globe; a configuration as part of the Multi-Scale Infrastructure for Chemistry and Aerosols version 0 (MUSICAv0) (Schwantes et al., 2022). More information about CAM-chem is in the supplementary section (S1).

In CAM-chem, aerosol hygroscopicity is represented with the kappa value (Petters and Kreidenweis, 2007) using the mixing rule (Stokes and Robinson, 1966). Kappa was calculated from the CAM-chem Aitken (0.015 – 0.053 µm) and accumulation mode (0.058 – 0.48 µm) outputs based on the volume fractions of the aerosol constituents (ε, Eq. 3) that were derived from their densities (Table S1). The following internally mixed aerosol species from CAM-chem were included in the analysis: organics (primary/hydrophobic, aged/hygroscopic, and secondary ($C_{15}H_{38}O_2$)), sulfate (NH_4HSO_4), sea salt, dust ($AlSiO_5$), and black carbon (primary/hydrophobic and aged/hygroscopic) (Tilmes et al., 2023). Some limitations in the calculation of kappa are that CAM-chem does not include nitrate aerosol, and that constant kappa values for primary and aged organics based on past work (Table S1) were used, even if it is known that kappa of organics varies with aging (Kuang et al., 2020). Kappa was also calculated from the submicrometer AMS and SP2 observations using the assigned species properties for available aerosol species in CAM-chem: aged organics, aged black carbon, and ammonium sulfate. Submicrometer sea salt and dust data are not available and were not included in the calculation for submicrometer kappa from observations.

$$\kappa_{chem} = \sum \kappa_i \, \varepsilon_i \qquad (3)$$

To enable a corresponding evaluation based on actual aerosol hygroscopicity observations, the f(RH) from CAMP[2]Ex were converted to kappa based on past studies (Brock et al., 2016b; Kuang et al., 2017; van Diedenhoven et al., 2022). The approximate wet (80%) and dry (20%) relative humidity values of the scattering measurements were used to convert f(RH) to an optical kappa (κ_{opt}) based on Equation 4 (Brock et al., 2016b; Kuang et al., 2017). This was approximated from the proportional relationship between the aerosol scattering cross section (which is the basis of f(RH)) and aerosol volume (the change of which is usually described as growth factor) which Brock et al. (2016b) in their study had associated with kappa. The optical kappa was converted to the chemical kappa (κ_{chem}) based on the slope of the relationship between κ_{opt} and κ_{chem} from Brock et al. (2016b). This method (Eq. 5) of converting κ_{opt} to κ_{chem} was also used by van Diedenhoven et al. (2022) for the f(RH) data for CAMP[2]Ex and is associated with 40% uncertainty (van Diedenhoven et al., 2022). The derived chemical kappa values for bulk aerosol particles are compared to the kappa calculated using the ZSR mixing rule from the submicrometer observations (AMS and SP2) and model outputs.

$$f(RH) = \frac{1 + \kappa_{opt} \frac{RH_{wet}}{100 - RH_{wet}}}{1 + \kappa_{opt} \frac{RH_{dry}}{100 - RH_{dry}}} \qquad (4)$$

$$\kappa_{chem} \approx \frac{\kappa_{opt}}{0.56} \qquad (5)$$

3. Results and Discussion

3.1 General Characterization of f(RH) for CAMP[2]Ex

3.1.1   Spatial Distribution of f(RH)

The f(RH) values in the CAMP[2]Ex campaign (Fig. 1a) had an interquartile range of values between 1.05 and 1.42 and were low (median of 1.24 for 143,107 1 s points) compared to other (Table 1) polluted marine environments (Titos et al., 2021). We note that the comparisons to other studies may be affected by the slight difference in relative humidity (f(RH=85%/RH=40% for Titos et al. (2021) and f(RH=82 ± 10%/RH<40% for this study) used to calculate f(RH). The distribution of f(RH) and ambient RH values is narrowest in the lowest altitudes (< 3 km), where most of the samples were taken (Fig. 1b). Both f(RH) and RH distributions become broader at higher altitudes, where there is a higher prevalence also for higher f(RH) values and lower RH values. Broadening of the f(RH) distribution at higher altitudes is at least partially attributed to lower dry scattering coefficients that result in increased uncertainty in the calculation of f(RH). The different aerosol sources (Fig. 1a) in the region also contribute to the range of measured f(RH), with transported emissions from more distant sources presumably more influential at the highest altitude ranges.

284
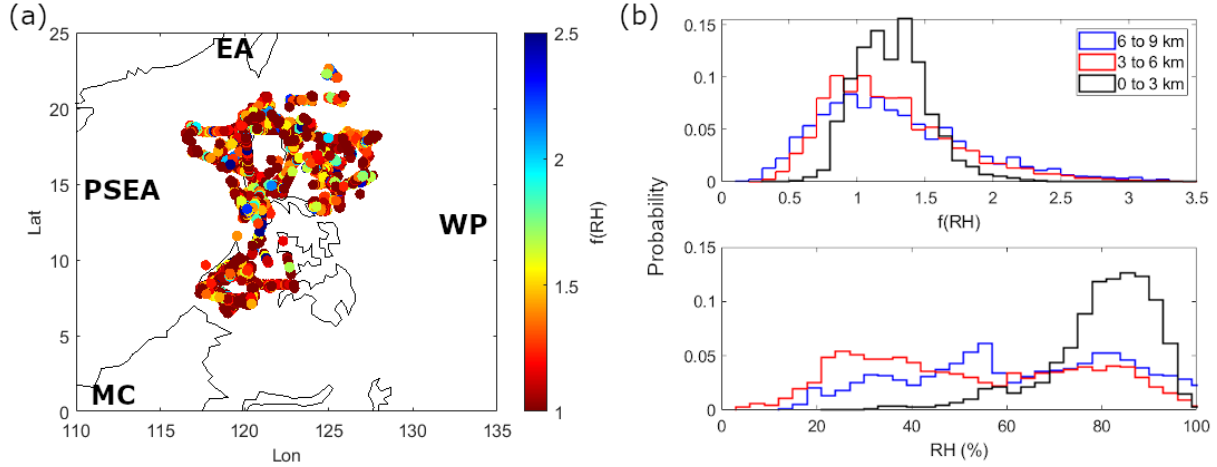
Figure 1. (a) Map showing flight locations during CAMP²Ex color coded by f(RH) 1 s values and approximate locations of the air mass sources (black text) identified by Hilario et al. (2021) that affected CAMP²Ex: Maritime Continent (MC), East Asia (EA), peninsular Southeast Asia (PSEA), and the West Pacific (WP) (PSEA is farther west at ~105°E and EA extends farther north) of air mass sources (Hilario et al., 2021) around the region. (b) Histograms of f(RH) and relative humidity (RH) for three altitude bins with the following counts: $n_{(0\ to\ 3\ km)}$: 139,026, $n_{(3\ to\ 6\ km)}$: 10,321, and $n_{(6\ to\ 9\ km)}$: 7,260.

The lowest median f(RH) (1.05 with Q1 and Q3 of 0.94 and 1.2) is from air masses traced to the MC (Fig. 2a), which coincide with influence from smoke particles. The air mass from EA (Fig. 2a) has the narrowest range of values (Q1: 1.28, median (Q2): 1.38, Q3: 1.47) compared to other air masses, likely representative of urban aerosol particles. The highest median f(RH) (1.49 with Q1 and Q3 of 1.26 of 1.73) are from air masses with back trajectories from the WP (Fig. 2a), likely due to marine aerosol particles interacting with particles from the MC and other regional sources. This mixing of the otherwise clean marine air with regional pollution sources effectively decreases aerosol hygroscopicity and this type of environment is often called a polluted marine environment (Titos et al., 2021).

Most (98%) of the f(RH) data were calculated for observations below 3 km (Fig. 2b), due to the relatively clean free troposphere in the region. Median f(RH) values generally decrease with altitude in the lower 3 km. An increase in median f(RH) is observed between 4 – 6 km (median from 1.14 to 1.32), where the contribution of the mixed air mass ("Other") is most dominant. The f(RH) values decrease above 6 km to the lowest median f(RH) (1.07) between 8 – 9 km, where air masses are generally from Other and the MC.

Latitudinally (Fig. 2c), f(RH) is lowest nearest Borneo in the MC (median of 0.95 to 1.07 in the regions from 6.85° N – 10.25° N), coincident with the dominant influence of biomass burning. There were active fires in the area during the time samples were taken from this latitude. f(RH) is highest in the northern Philippines (median of 1.33 to 1.44 in the regions from 18.75° N – 22.15° N), where the influence of WP and EA air was most prevalent. This is consistent with the longitude data (Fig. 2d), which exhibit the lowest f(RH) values for longitudes (median of 1.02 to 1.18 in the regions from 117.95° E – 120.55° E) that had the highest MC contribution. The highest f(RH) is observed in longitudes (median of 1.38 to 1.40 in the regions west of 116.65° E and east of 123.15° E) that were more associated with the northern Philippines (Fig. 1a). To delve deeper into our analysis, we discuss next the size and composition data.

310

311
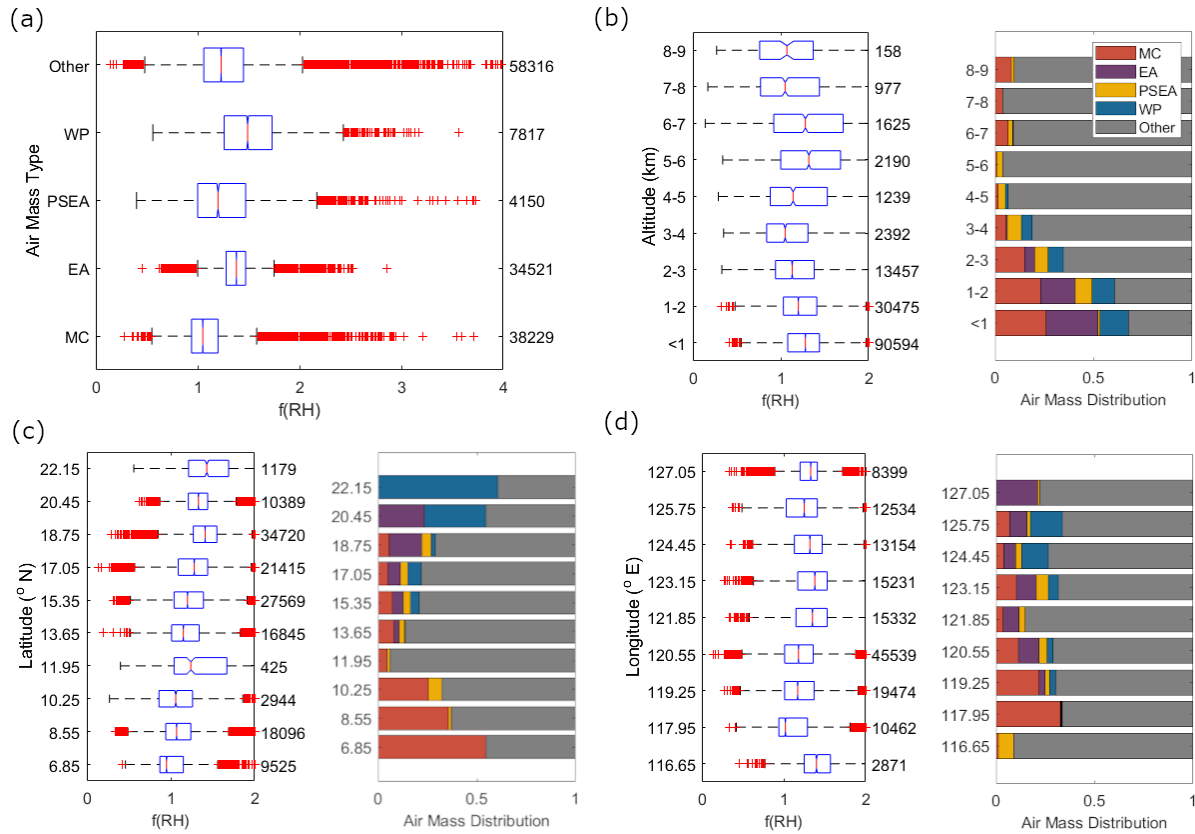
Figure 2. Distribution of 1 s f(RH) data during the CAMP²Ex field campaign for relevant **(a)** air masses, **(b)** altitude, **(c)** latitude, and **(d)** longitude levels and corresponding stacked bars of air mass contributions for panels b - d. The **(a)** air mass types are from Hilario et al. (2021). The numbers to the right of the notched boxplots are the counts, and the **(b – d)** bars to the right of the boxplots show the fractional contribution of each air mass type to the total number of air masses in the specific location. The y-values for **(c-d)** latitude and longitude are the midpoints of the specific coordinate bins.

3.1.2   f(RH) Relationships with Size and Composition

The relative size of particles per air mass can be inferred from the extinction Ångström exponent (AE), which relates the extinction of light at specific wavelengths to particle size (Ångström, 1929). Since scattering is the dominant component of extinction, the scattering Ångström exponent (SAE) is often used to relate to particle size, where larger SAE suggests smaller particles. The median SAE values (Fig. 3a) are similar and between 2.09 (MC with Q1 and Q3 of 1.92 and 2.26) to 2.16 (Other with Q1 and Q3 of 1.75 and 2.32) for four of five air masses, indicative of smaller particles. The WP has a median value of 1.37 (with Q1 and Q3 of 1.05 and 1.88), suggestive of the presence of a mixture of accumulation-mode and coarse-mode particles (SAE < 1 occurs for large particles like sea salt and dust) (Schuster et al., 2006; Bergstrom et al., 2007). Past studies have suggested that biomass burning particles exhibit SAE values greater than 1.4, which does not discount the fact that most of the f(RH) data collected during CAMP²Ex is possibly impacted by biomass burning.
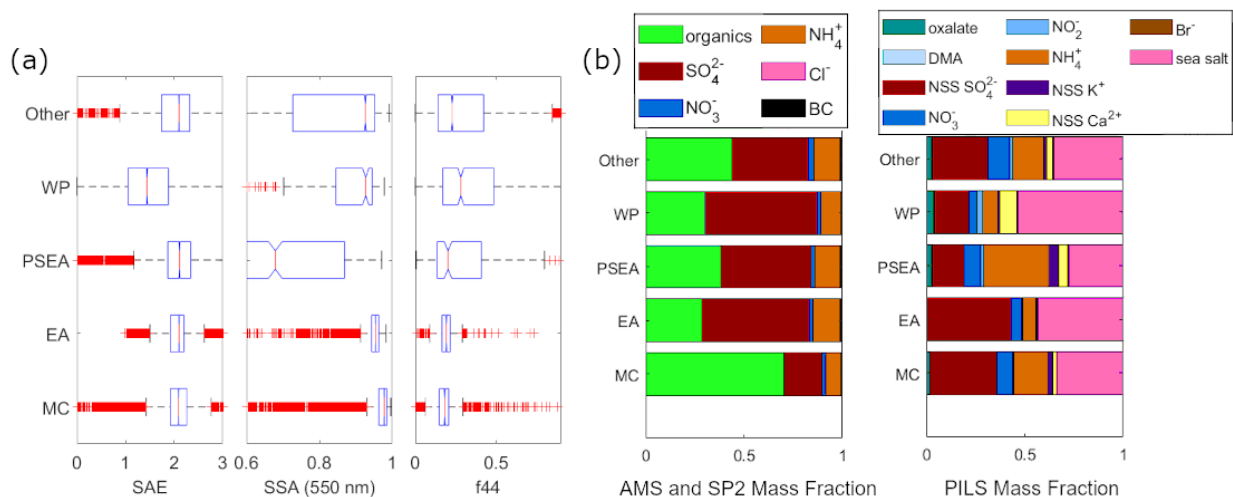
Figure 3. (a) Boxplots of 1 s scattering Ångström exponent (SAE), single scattering albedo (SSA, 550 nm), and ratio of the mass spectral marker m/z 44 marker relative to total organic mass (f_{44}) and (b) (left) submicrometer mean organic, SO_4^{2-}, NO_3^-, NH_4^+, Cl^-, and black carbon (BC) mass fractions and (right) bulk (< 5 μm) oxalate, dimethylamine (DMA), non-sea salt SO_4^{2-}, NO_3^-, NO_2^-, NH_4^+, non-sea salt K^+, non-sea salt Ca^{2+}, Br^-, and sea salt mass fractions per air mass (Hilario et al., 2021).

One of the indicators of biomass burning in Southeast Asia is organic matter (Adam et al., 2021). The MC air mass (Fig. 3b) has the greatest (71%) mass fraction of organics among the air masses and the highest median SSA (0.98 with Q1 and Q3 of 0.96 and 0.99) (Fig. 3a) that suggests more scattering, rather than absorbing, particles (Moosmüller and Sorensen, 2018). This is consistent with observations from field work in tropical peatland fire in Southeast Asia, where particles were mostly from smoldering combustion and were moderately absorbing, with brown carbon dominating absorbance (Stockwell et al., 2016). Smoldering combustion, which is more common in the Maritime Continent (Reid et al., 2013), is known to produce less elemental carbon (Reid et al., 2005) and potassium (Robinson et al., 2004) compared to flaming combustion. Biomass burning activities were active in the MC during the field campaign (Reid et al., 2023). The MC air mass also has the lowest f_{44} median values (0.18 with Q1 and Q3 of 0.15 and 0.21) (Fig. 3a) suggesting it is the least-oxidized and least photochemically-aged air mass and thus closest to the source compared to other air masses. Chen et al. (2022) who studied tropical peat smoldering (similar to those in MC) showed that primary organics were not oxidized (f_{44} < 0.02) while secondary organics were highly oxidized, that oxidation increases f_{44} (oxidized organics: 0.01 < f_{44} < 0.11), and that high RH speeds up the oxidation process especially for smaller particles (~100 nm) (Chen et al., 2022). In the U.S., as another example, f_{44} from wildfire plumes up to 8 hours old did not exceed 0.12 (Garofalo et al., 2019). The high RH during CAMP²Ex (Fig. 1b) likely led to the increased oxidation of secondary organics resulting in median f_{44} values that are relatively high (for all air masses even in MC), suggesting that most of the particles sampled during CAMP²Ex are aged. The high organic mass fraction is consistent with the MC having the lowest median f(RH) as organics are known to reduce aerosol hygroscopicity (Kalberer, 2014; Sorooshian et al., 2017; Shingler et al., 2016a).

There is an inverse relationship between hygroscopicity and organic mass fraction data that is most evident in f(RH) values collected within the boundary layer (< 3 km) during CAMP²Ex (Fig. 4a). Those data points that have the highest organic mass fraction values (> 0.6) are also associated with CO concentrations (> 250 ppb) that are typically

356 associated with biomass burning (Shingler et al., 2016a) and are mostly from the MC area (Fig. 4b). The slope of the

357 inverse relationship between f(RH) and organic mass fraction is most steeply negative (-0.81) for the air masses

358 coming from EA (Fig. 4c) .

359
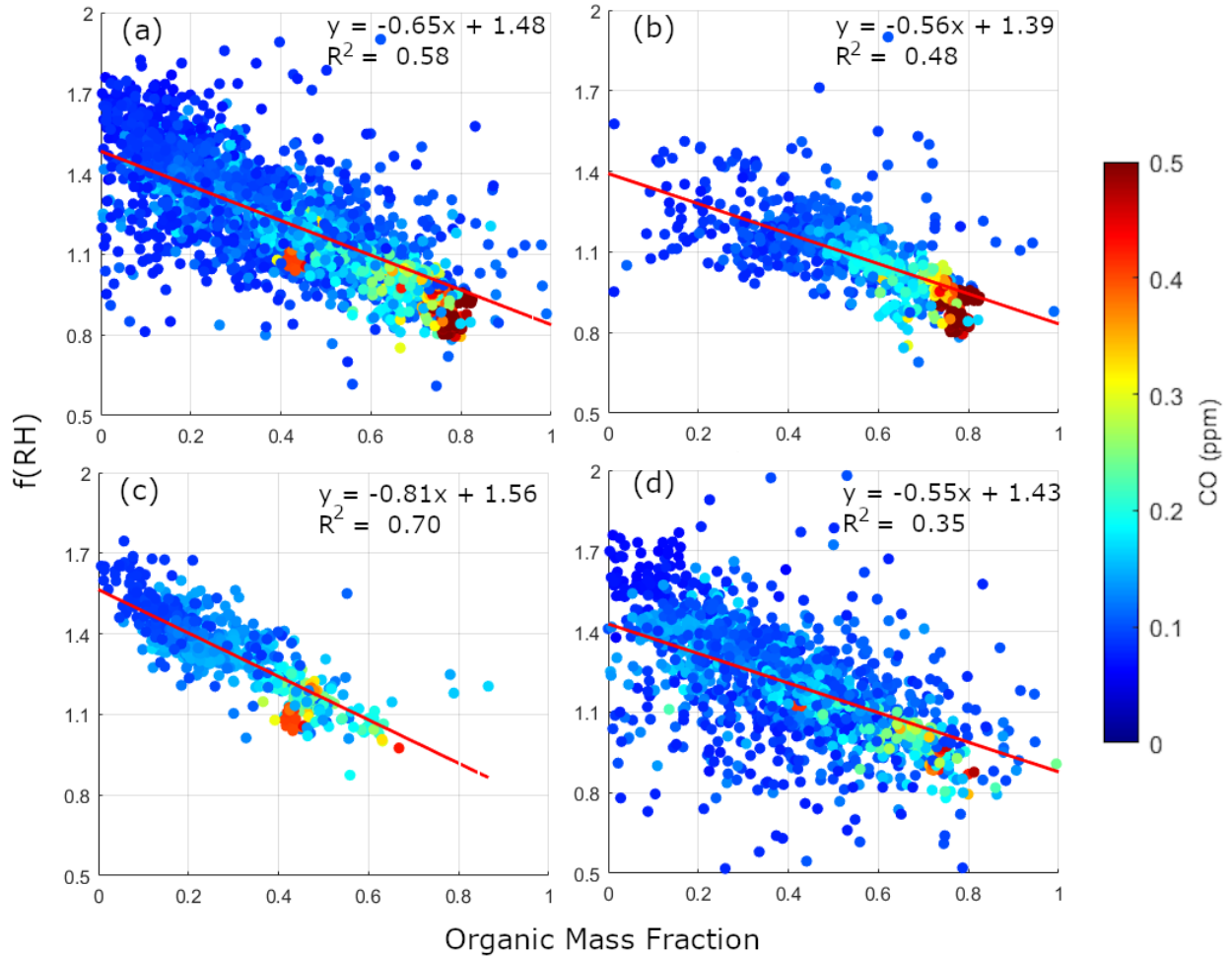
Figure 4. (a-d) Scatter plots of 30 s averaged f(RH) and corresponding organic mass fraction contribution to total submicrometer aerosol mass (sum of organic, SO_4^{2-}, NO_3^-, NH_4^+, Cl^-, and black carbon (BC) mass concentration) for (a) all data collected at altitudes below 3 km and (b-d) for air masses coming from (b) the Maritime Continent (MC), (c) East Asia, and (d) Other. The dots are colored by their CO concentration.

364 The highest median f(RH) values are from the WP and EA air masses (Fig. 2a). Both have lower organic mass

365 fractions (0.29 and 0.30, respectively) compared to other air masses and are therefore expected to have higher f(RH)

366 based on Fig. 4. The WP air masses have coarser particles, based on their SAE values (Fig. 3a), and have a marine

367 origin (with higher DMA mass fraction, Fig. 3b) with high sea salt fraction (54%, Fig. 3b), contributing to it having

368 the highest median f(RH) amongst the air masses. The WP air masses appear to have interacted with aged organic

369 particles from biomass burning and industry including fine absorbing particles potentially from industry and dust

370 owing to its relatively high median f_{44} (0.26 with Q1 and Q3 of 0.17 and 0.48) and low median SSA (0.93 with Q1

371 and Q3 of 0.85 and 0.95). Particles with predominantly clean marine sources tend to have higher ($\geq$ 0.97) SSA

372   (Dubovik et al., 2002), thus the WP data suggest a polluted marine source (Lacagnina et al., 2015). Though, we note

373   that the air masses from the WP have relatively low scattering and absorption coefficients and that these could have

374   affected the calculations for SSA. EA air exhibits the highest non-sea salt sulfate mass fraction (0.43) (Fig. 3b) that,

375   along with its predominantly fine particle size and median SSA (0.95 with Q1 and Q3 of 0.94 and 0.96), strongly

376   suggests that it was transported from an urban source. Sulfate is a known industrial product of East Asia (Smith et al.,

377   2011; Li et al., 2017; Lorenzo et al., 2023).

378   Particles from PSEA have the lowest median SSA (0.68 with Q1 and Q3 of 0.55 and 0.87) (Fig. 3a). This suggests the

379   presence of more absorbing particles relative to scattering, possibly including elemental carbon and aged dust. Based

380   on the PSEA air masses having the highest non-sea salt potassium mass fraction (0.05, Fig. 3b) the particles could be

381   from biomass burning. It is well-documented that dust can be entrained in smoke plumes due to reasons such as

382   turbulent mixing around flames and burn fronts (Palmer, 1981; Kavouras et al., 2012; Maudlin et al., 2015; Schlosser

383   et al., 2017). Dust from East Asia and biomass burning from PSEA have been observed to be mixed in the boreal

384   spring in Taiwan (Dong et al., 2018), and though CAMP²Ex sampled during a different season, it is still possible that

385   this mixing of East Asian dust and PSEA biomass burning could have occurred and impacted the CAMP²Ex region

386   during the field campaign.

387
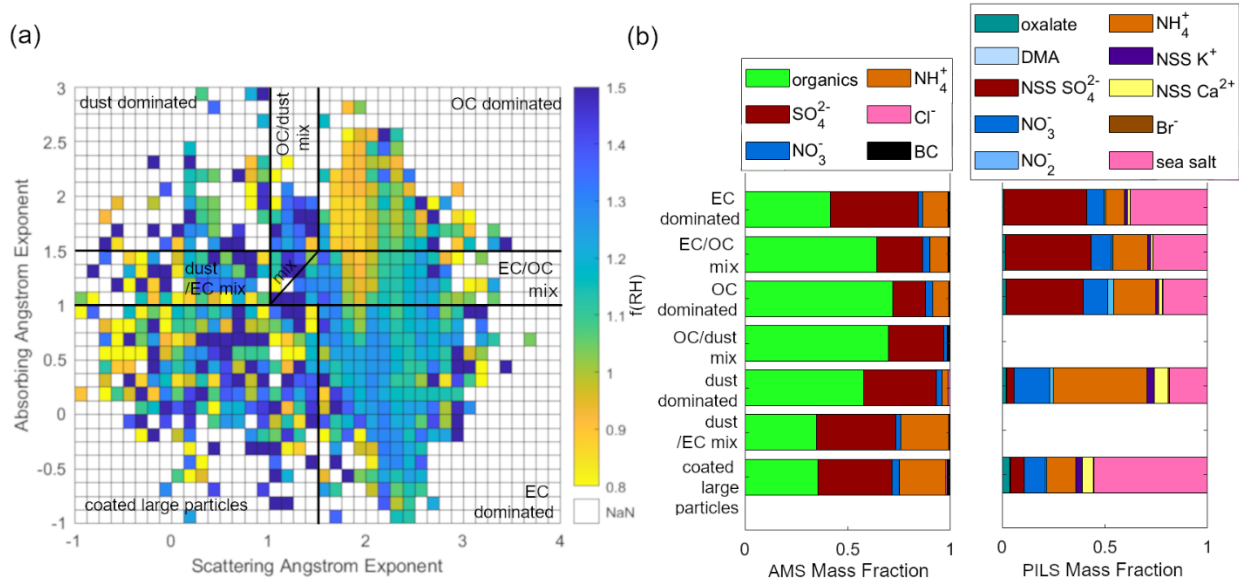
388   **Figure 5. (a) Median f(RH) of data points with absorbing Ångström Exponent (AAE) and scattering Ångström Exponent**
389   **(SAE) values that correspond to suggested aerosol types from past studies (Cazorla et al., 2013) with following counts and**
390   **bulk median f(RH) per aerosol type: EC dominated (16,908 and 1.19), EC/OC mix + mix (20,686 and 1.03), OC dominated**
391   **(1942 and 0.94), OC/dust mix (55 and 1.31), dust dominated (79 and 1.15), dust/EC mix (204 and 1.12), and coated large**
392   **particles (729 and 1.21). (b) (left) Submicrometer mean organic, SO4²⁻, NO3⁻, NH4⁺, Cl⁻, and black carbon (BC) mass**
393   **fractions and (right) available bulk (< 5 μm) oxalate, dimethylamine (DMA), non-sea salt SO4²⁻, NO3⁻, NO2⁻, NH4⁺, non-sea**
394   **salt K⁺, non-sea salt Ca²⁺, Br⁻, and sea salt mass fractions per aerosol type.**

395   Using the AAE and SAE with categorization determined by Cazorla et al. (2013), the f(RH) can be related to the types

396   of aerosols. Note that the median f(RH) values for the aerosol types may be slightly different than the raw 1 s f(RH)

397   data because the median f(RH) is only calculated for the aerosol types when both the scattering and absorbing

398   Ångström Exponent values are available. The highest median f(RH) of 1.31 (with Q1 and Q3 of 0.89 and 1.46) and

399   1.21 (with Q1 and Q3 of 0.88 and 1.68) are from the OC/dust mix and coated large particles aerosol types (Fig. 5),

400   respectively, though there are only 55 data points for the OC/dust mix so the aerosol classification for it may not be

401   as robust. The high f(RH) for the coated large particles is consistent with its largest bulk sea salt mass fraction (0.56)

402   (Fig. 5b) compared to other aerosol types, though they only make up 1.8 % of the total number of particles. Dust

403   dominated particles make up only 0.05% of the total number of particles and had the highest non-sea salt calcium and

404   a median f(RH) of 1.15 (with Q1 and Q3 of 0.94 and 1.43).

405   Most of the aerosol particles (< 5 µm dry diameter and 93% of all particles) collected during the CAMP^{2}Ex field

406   campaign have optical properties (Fig. 5a) that resembled EC/OC mix + mix (in this case we combined the sub-

407   categories of EC/OC mix and mix) (51%) and EC dominated (42%) aerosol types. These carbonaceous particles are

408   less hygroscopic, and their dominance helps to explain the low median f(RH) in the CAMP^{2}Ex region. The EC

409   dominated particles have the third highest median f(RH) at 1.19 (with Q1 and Q3 of 1.05 and 1.33), which is unusual

410   because EC is known to be hydrophobic. Compositional data sheds some light on this, because the particles classified

411   as EC dominated have higher submicrometer sulfate (0.43) and bulk sea salt (0.38) mass fractions (Fig. 5b) compared

412   to particles classified as OC (0.16 and 0.22) and dust dominated (0.35 and 0.19), which are known to have low

413   hygroscopicity in general. This mixing of sulfate and sea salt with EC dominated particles increases their bulk f(RH).

414   The EC dominated particles come from the EA, MC, and Other air masses. East Asia is a known sulfur source and

415   shipping contributes to sulfate in the region (Miller et al., 2023). Peat smoke particles from MC have also been found

416   in past studies to have sulfate mixed with carbonaceous species (Nakajima et al., 1999), where up to ~20% of the mass

417   fraction of secondary organic aerosol from lab experiments on peat burning was attributed to sulfate (Chen et al.,

418   2022).

419   The OC dominated type have the highest submicrometer organic mass fraction (0.72) and a median f(RH) of 0.94

420   (with Q1 and Q3 of 0.85 and 1.06), which is consistent with the expected effect of organics to lower hygroscopicity.

421   The median f(RH) values below 1, though, are counterintuitive given that the presence of moisture in the region is

422   thought to generally increase the particle size and consequently the amount of aerosol light scattering. Data where

423   f(RH) is less than unity have been observed in past studies due to a number of suspected factors including (but not

424   limited to) volatilization effects, changes in optical properties during humidification, and particle restructuring

425   (Shingler et al., 2016b).

426

427
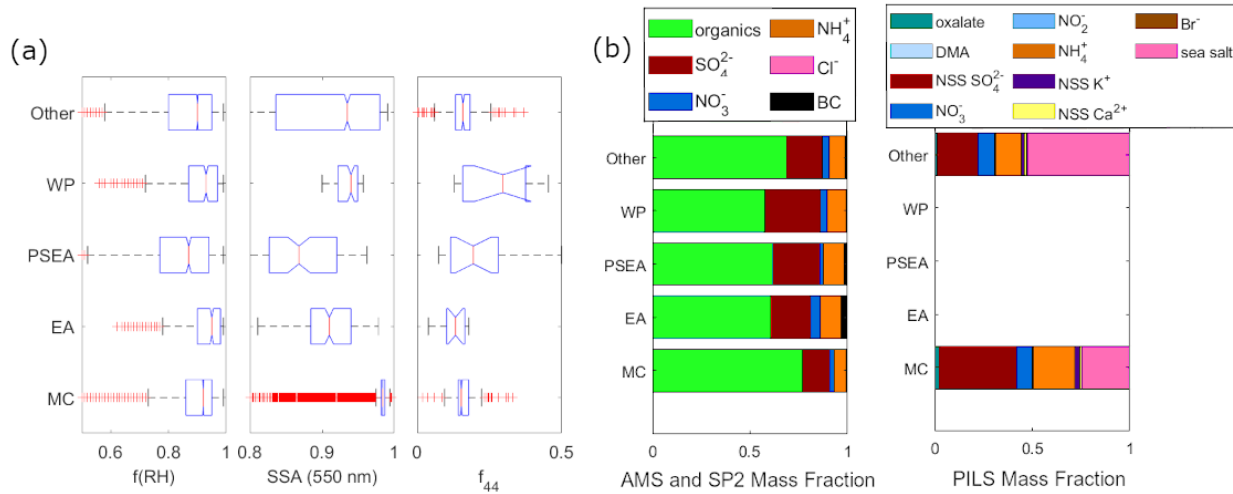
Figure 6. (a) Boxplots of 1 s f(RH) < 1 (MC: 14,612, EA: 473, PSEA: 986, WP: 483, and Other: 9919 counts) and the corresponding single scattering albedo (SSA, 550 nm) and ratio of the mass spectral marker m/z 44 marker relative to total organic mass (f₄₄) and (b) (left) submicrometer mean organic, SO_4^{2-}, NO_3^-, NH_4^+, Cl^-, and black carbon (BC) mass fractions and (right) available bulk (< 5 μm) oxalate, DMA, non-sea salt SO_4^{2-}, NO_3^-, NO_2^-, NH_4^+, non-sea salt K^+, non-sea salt Ca^{2+}, Br^-, and sea salt mass fractions per regional air mass (Hilario et al., 2021) for times with f(RH) < 1.

To investigate aerosol characteristics when f(RH) is < 1, we plot the f(RH) box plots from each of the regions for data points where f(RH) < 1 (Fig. 6a). There are several instances (26,473 times or 19% of the time for the whole campaign) when the f(RH) was below 1. In general, 30 s resolution organic mass fractions greater than 0.75 correspond to sub-1 f(RH) (Fig. 4a). The most prevalent regional air mass association for sub-1 f(RH) is with the MC air masses (f(RH) < 1 from the MC was 56% of all data). The mean organic mass fraction is dominant (0.57 – 0.77) and almost doubled compared to the whole campaign (Fig. 3b), for all the air masses with sub-1 f(RH) (Fig. 6b). Mean organic mass fraction is highest for the MC (0.77) air mass. The organics from the sub-1 f(RH) data are the least aged throughout the campaign for the MC, PSEA, and Other air masses (Fig. 6a). The CAMP²Ex data offer an opportunity to inspect the prevalence of such values and to see what factors coincide with such situations. However, the unique sample make-up of the particles in the CAMP²Ex region makes other reasons, including sample losses due to volatilization, also plausible (Reid et al., 2023). Shingler et al. (Shingler et al., 2016b) also observed such sub-1 values for both f(RH) and the humidified diameter growth factor g(RH) in air masses enriched with carbonaceous components over North America.

The most dominant aerosol types for the sub-1 f(RH) data are the carbonaceous ones (96%) (Fig. 5b), with the EC/OC component contributing the most: EC/OC mix + mix (the combined sub-categories of EC/OC mix and mix) (68%), EC-dominated (18%), and OC-dominated (10%). Both bulk ammonium and sulfate mass fractions for the MC also are higher for the sub-1 f(RH) cases (Fig. 6b) compared to the whole campaign (Fig. 3b, PILS), while the bulk sea salt mass fraction was lower. The bulk sea salt mass fraction of the Other category (Fig. 6b) increases for the sub-1 f(RH). Most of the particles contributing to the sub-1 f(RH) are fine particles (median Ångström Exponent ~2, Fig. 6a) with

452 more reflective characteristics (SSA ≥ 0.90) compared to data for the entire campaign. To understand more about sub-

453 1 f(RH), we will look at a selected case in the succeeding section.

3.2 Case Studies

3.2.1 Sub-1 f(RH) from Biomass Burning Smoke

456 The chosen case study is part of a flight on 16 September 2019 that occurred closest to the Maritime Continent, which

457 is the source of the air masses that had the most counts of sub-1 f(RH) (Section 3.1.2). This flight coincided with an

458 active biomass burning event on 14 September 2019 (NASA, 2020) and fire hotspots in the Maritime Continent were

459 numerous throughout September 2019 (Othman et al., 2022). The back trajectories at 01:00 UTC, when the aircraft

460 began to make measurements closest to the surface (~300 m altitude) and perpendicular to the wind, all come from

461 the southwest of the aircraft location (Fig. 7a), in the direction from where biomass burning emissions were being

462 transported. Details about the flight and conditions during this case study are found in Crosbie et al. (2022). In their

463 study they note the smoke to be from Kalimantan with an age between 48 and 72 h. Consistently low f(RH) (all below

464 1, Fig. 7b) values were observed for a little less than an hour, until the aircraft began its ascent (Fig.7b). The aerosol

465 mass concentrations of >70 µg m^{-3} were among the highest in the entire field campaign and were dominated by

466 organics (Fig. 7b).

467
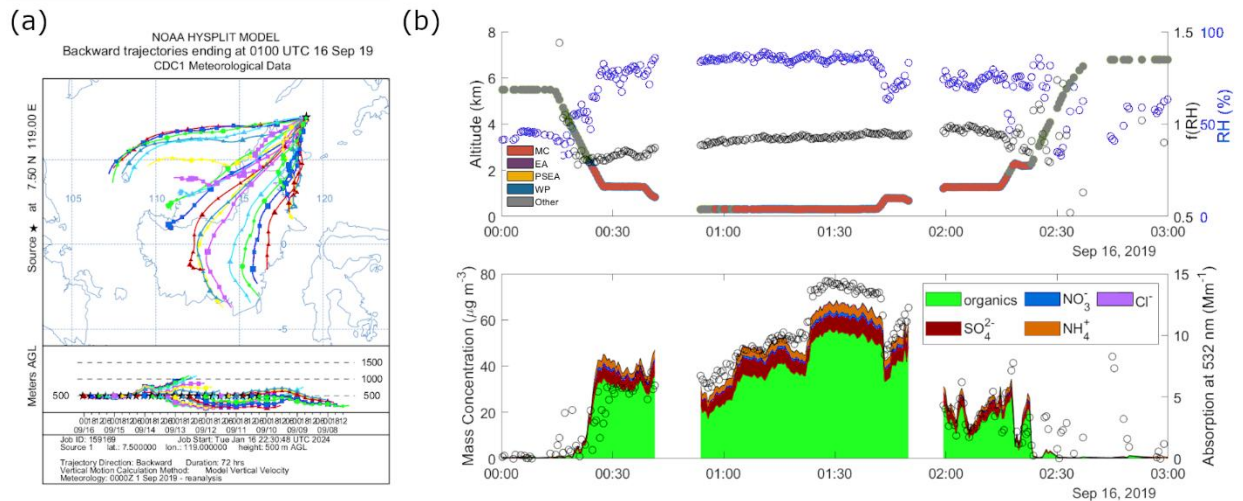
468 **Figure 7. Case study of sub-1 f(RH) on 16 September 2019. (a) Five-day back trajectories at the approximate flight location**
469 **at 01:00 UTC. (b) (top) Time series plots of altitude colored by regional air mass, f(RH) in black circles, and RH (blue**
470 **circles), and (bottom) aerosol mass concentrations from the AMS and absorption at 532 nm (black circles) during one of**
471 **the flight legs closest to the surface from 00:00 to 03:00 UTC.**

472 The sub-1 f(RH) during the lowest altitudes of the aircraft, from 01:00 to 01:40 UTC, are correlated with

473 approximations of the submicrometer particle effective density (Fig. 8a). Absorption measurements along with back

474 trajectories linked to active fires point to the increasing presence of EC and brown carbon with increasing particle

475 density (even if there were no valid EC measurements for this specific time). Submicrometer number concentration,

476 dry absorption (532 nm), organic mass fraction, and single scattering albedo are highest for the smallest effective

477 density values for sub-1 f(RH) (Fig. 8b) during the entire campaign, likely due to the presence of EC and OC. This is

478 consistent with the most dominant aerosol type during the field campaign, which is a mix of elemental and organic

479 carbon based on SAE and AAE values. The dataset cannot be used to prove particle restructuring and very likely the

480 sub-1 f(RH) values are due to other factors since particles' history included passes through humid areas where

481 restructuring presumably would have already occurred prior to reaching the aircraft. In addition, smoldering from

482 peat, which is dominant in the MC fires (Reid et al., 2023), is known to produce homogenous spheres, with no voids,

483 that are similar to OC particles (Pokhrel et al., 2021), making restructuring unlikely to be the dominant mechanism to

484 explain our findings. However, we present these results for the sake of documenting a Southeast Asia case of these

485 unusual events occurring in EC/organic-rich air masses similar to past work (e.g., Shingler et al., 2016b and references

486 therein) to emphasize that these events occur throughout the world and to motivate more research into the matter.

487
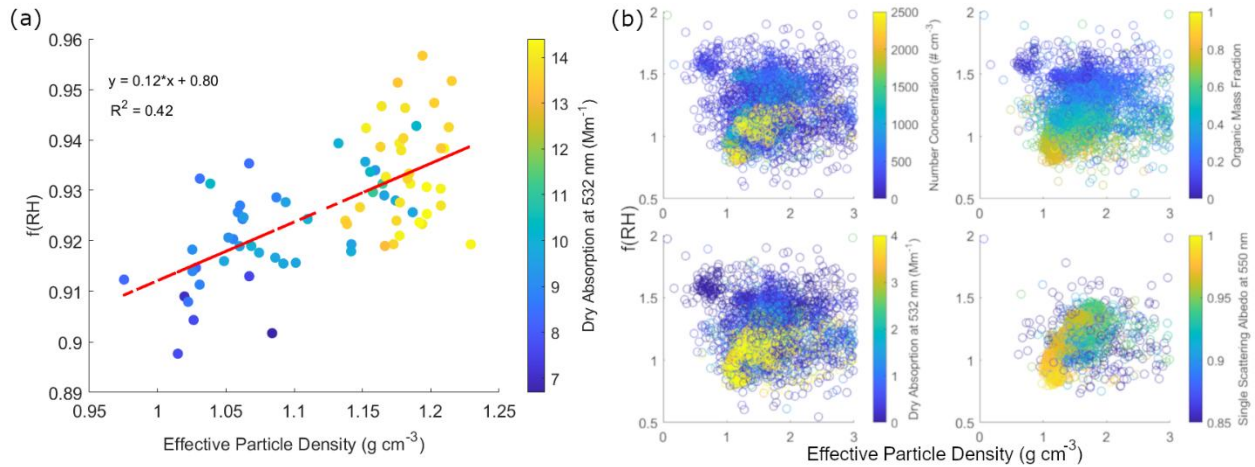
488 **Figure 8. 30 s f(RH) and effective particle density plots for (a) 16 September 2019 from 01:00 to 01:40 UTC colored by dry**
489 **absorption at 532 nm, and (b) for the entire CAMP²Ex field campaign and colored by (clockwise from top left) LAS number**
490 **concentration of particles with diameters between 100 and 1000 nm, organic mass fraction, single scattering albedo at 550**
491 **nm, and dry absorption at 532 nm.**

492 Smoke particles are known to have a range of density values, depending on their degree of atmospheric aging, affecting

493 their size, and the processes they undergo. The effective particle density is usually lower for biomass burning particles

494 from smoldering that have larger diameters (Pokhrel et al., 2021), compared to flaming. Freshly emitted smoldering

495 particles have effective densities from 1.03 g cm^{-3} to 1.21 g cm^{-3} that do not vary much with diameter based on a

496 laboratory study (Pokhrel et al., 2021). Our calculated values fall within this range (Fig. 8). This adds confidence to

497 our observation that organics (brown carbon), which dominate smoldering emissions, are the major contributors to the

498 sub-1 f(RH). Both aerosol hygroscopicity and effective particle density are important for properly modeling cloud

499 condensation nuclei, one of the most important factors in aerosol-cloud interactions.

500 **3.2.2 Vertical Transport**

501   The vertical distribution of aerosols affects cloud formation, we investigate this through two cases of aerosol vertical
502   transport. The vertical transport cases were identified from averages of the available vertical profiles made during
503   CAMP²Ex. A large-scale event (01:53 to 06:20 UTC 20 Sep 2019) north of Luzon, Philippines, due to a tropical
504   cyclone, and a smaller-scale event (02:55 to 06:02 UTC 24 Sep 2019) east of Luzon, due to shallow convection were
505   chosen for the case studies. The measured median CO mixing ratio was used as a tracer for vertical transport (Kar et
506   al., 2004). An increase in the median CO mixing ratio at higher altitudes along with multi-level winds from a similar
507   direction were the main criteria used to identify the cases.

508   Northerly to northwesterly winds are the dominant source for the first case (Fig. 9a) influenced by tropical cyclone
509   Tapah (TC Tapah's center was ~600 km northeast of the aircraft location). This suggests the influence of East Asia
510   on the sample as described in Crosbie et al. (2022), where the meteorology is discussed in more detail. There is a
511   general decrease in f(RH) from the lower levels that follows a similar trend to the decrease in total mass (Fig. 9b) and
512   sulfate mass fraction. Sulfate is hygroscopic so it is understandable that the f(RH) decreased with altitude as the sulfate
513   decreased. The increase in CO between 6-7 km (Fig. 9b) suggests vertical transport aloft and was accompanied by a
514   subsequent decrease in f(RH) and ammonium mass fraction and increase in organic mass fraction (Fig. 9b) between
515   6-8 km. This is consistent with analysis in previous sections, which show decreased f(RH) with increased organic
516   mass fractions.

517   Accompanying the general decrease of f(RH) with altitude are decreasing submicrometer median volume size
518   distribution (VSD) magnitudes and volume weighted average diameters (Fig. 10). Possible reasons for these trends
519   are that larger hygroscopic particles, such as sulfate (which make up the largest mass fraction at lower levels), were
520   scavenged (especially at lower altitudes) and/or activated into cloud drops, leaving the smaller particles behind.
521   Submicrometer aerosol mass also decreases with altitude, with values below 1 µg m^{-3} (Fig. 9b). There is a slight
522   increase in VSD magnitude from 6-8 km compared to 4-6 km, and especially at larger diameters, broadening the VSD
523   curve which may suggest cloud processing (Eck et al., 2012). Though sulfate enhancements have traditionally been
524   the marker for cloud processes (Barth et al., 2000; Faloona, 2009), more recent studies have observed potential cloud
525   processing cases with increased organics (i.e. Wonaschuetz et al., 2012; Dadashazar et al., 2022). This case could
526   thus be showing vertically transported organic matter that has possibly affected or was affected by the clouds between
527   6-7 km. Another observation is the increase of ammonium and nitrate mass fractions above 4 km (Fig. 9b). There is
528   no corresponding valid f(RH) data, and we can only infer based on the CO profile that begins to shift toward a more
529   positive slope with increasing altitude that this increase in ammonium could also be associated with cloud processing.
530   Ammonia is abundant in East Asia (Pawar et al., 2021) And although there are still limited studies, the scavenging
531   efficiencies of organics and ammonium (compared to sulfate) could also be contributing to their increasing mass
532   fractions with altitude (Yang et al., 2015; Hilario et al., 2025).

533
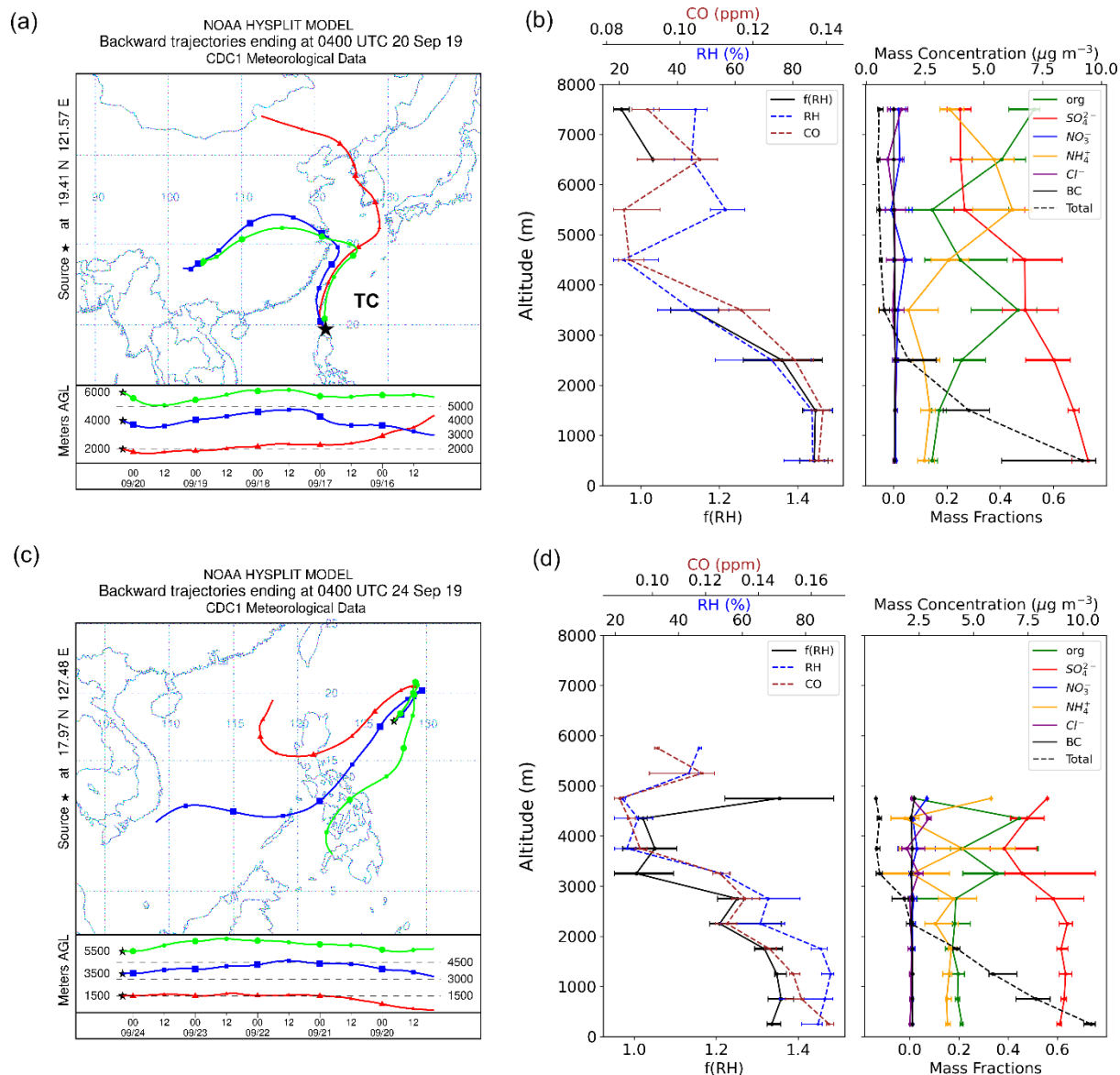
Figure 9. Case studies of (a-b) tropical cyclone-induced convection on 20 September 2019 and (c-d) shallow convection on 24 September 2019. (a) Five-day multi-level back trajectories from the average location of the aircraft from 01:53 to 06:20 UTC with the approximate TC center location and (b) vertical profiles (median, 25 and 75th percentiles) of (left) f(RH), relative humidity (RH), and CO mixing ratio and (right) submicrometer mass fractions of organics, sulfate, nitrate, ammonium, and black carbon and sum of mass concentrations from AMS and SP2 (dashed black line) for 1 km altitude bins, (c) five-day multi-level back trajectories from the average location of the aircraft from 02:55 to 06:02 UTC, and (d) vertical profiles of f(RH), relative humidity (RH), CO mixing ratio, and submicrometer mass fractions and sum of mass concentrations from AMS and SP2 for 0.5 km altitude bins.

542
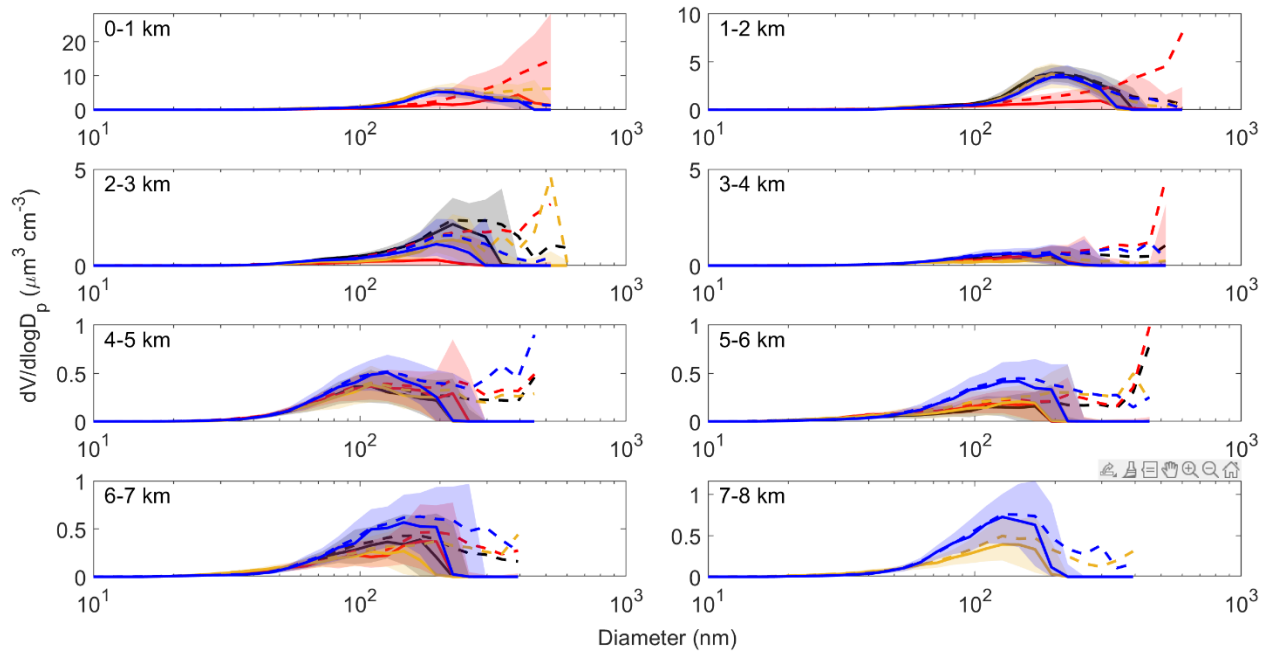
Figure 10. Median (solid line), mean (dashed line), and 25th to 75th percentiles (shaded area) of volume size distributions of submicrometer particles (FIMS) every 1 km altitude for the case study of tropical cyclone-induced convection on 20 September 2019 from 01:53 to 06:20 UTC. The colors represent four separate vertical profiles, where black was from 01:35 to 02:19 UTC, red was from 03:40 to 04:44 UTC, yellow was from 04:59 to 05:27 UTC, and blue was from 05:52 to 06:20 UTC.

The second case, the shallow cumulus case on 24 September 2019 (Hilario et al., 2025), has multi-level wind trajectories initially from the West Pacific in the northeast direction, which appear to have come from the Philippines and the general southwest direction from two days before (Fig. 9c). The most evident increase in CO (Fig. 9d) is observed between 5-5.5 km, at an altitude lower than the previous case. Both RH and f(RH) have a similar trend to CO throughout the vertical profile, which slightly follows the trend of sulfate mass fraction. This is observed especially in the lower levels (until ~2 km) where RH and f(RH) are relatively steady, even with a large decrease in total aerosol mass.

At higher altitudes, above 4.5 km, f(RH) increases to a greater degree with decreased organic mass fraction and increased sulfate mass fraction (Fig. 9d), possibly due to cloud processing. Like the first case, the VSD plots (Fig. 11) for this case show decreasing VSD magnitudes and volume weighted average diameters with increasing altitudes. The broadening of the VSDs above 3 km, concurrent with the increased decreased sulfate mass fraction, likewise suggests cloud processing. There is a known sulfate source, a power plant in western Luzon, in the Philippines that is along the path of the 1.5 km back trajectory (Fig. 9c) and may possibly contribute to sulfate in the region (Lorenzo et al., 2023). It is possible that this and other sulfate sources in the region, such as those from ships (Miller et al., 2023), are being transported vertically and affecting aerosol hygroscopicity in the areas where there is shallow convection.

563
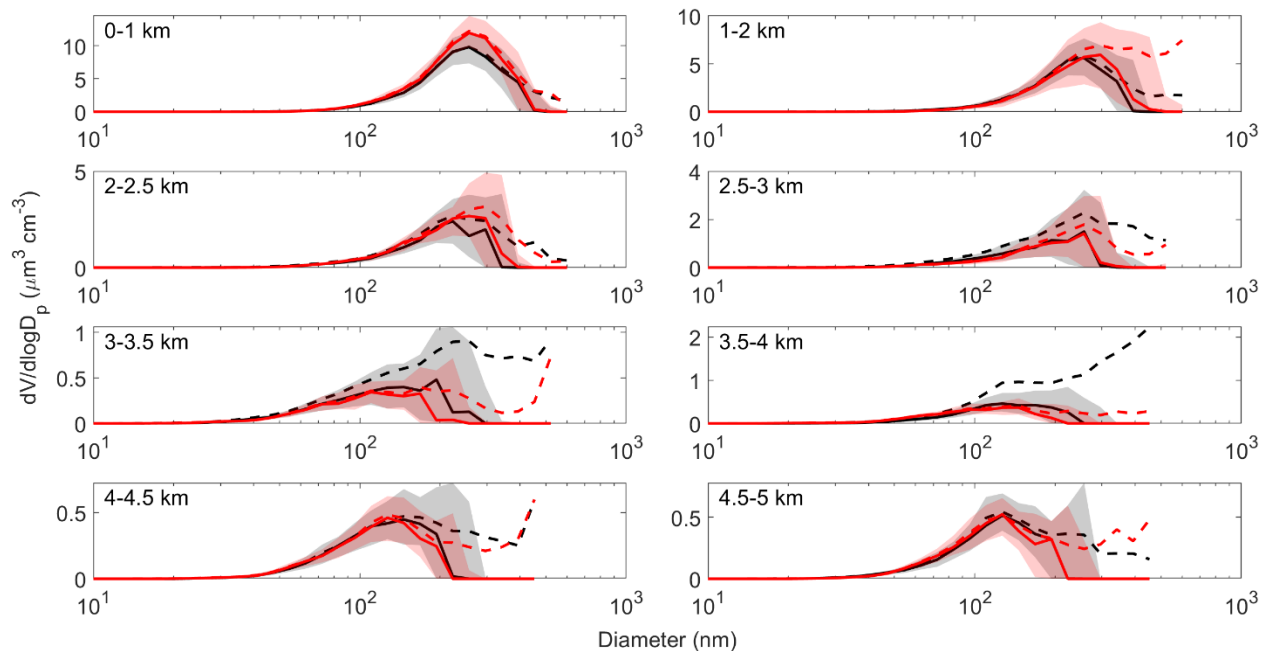
Figure 11. Median (solid line), mean (dashed line), and 25th to 75th percentiles (shaded area) of volume size distributions of submicrometer particles (FIMS) in 0.5-1 km altitude increments for the case study of shallow convection on 24 September 2019 from 02:55 to 06:02 UTC. The colors represent two separate vertical profiles, where black was from 02:55 to 04:07 UTC and red was from 05:42 to 06:02 UTC.

In summary, for both cases vertical transport in cumulus clouds correspond to higher f(RH) with lower organic mass fractions or increased sulfate mass fractions, at cloud outflow altitudes. At slightly higher altitudes, increasing organics with decreasing ammonium decrease f(RH) for the tropical cyclone case. The VSD magnitudes and the averaged diameter of the aerosol size decrease from cloud base to cloud outflow altitudes, with the VSDs broadening likely due to cloud processing. The understanding and representation of the vertical transport or aerosols due to the tropical cyclone and shallow convection and their role in aerosol-cloud interaction is further investigated as we evaluate modeled data using the two cases that we have just discussed.

3.2.3 Model Evaluation

To give regional context to the cases, we begin the discussion of model evaluation with the horizontal distribution of the modeled (~111 km resolution) near-surface aerosol hygroscopicity (kappa: calculated from the volume fractions and kappa values (Eq. 3) of the modeled submicrometer aerosol species as described in 2.3.2) and winds within the CAMP^{2}Ex domain. We will compare the model kappa values to kappa from different regions around the world based on previous studies. Subsequently, we will discuss how the modeled submicrometer kappa at different vertical levels compare to the kappa derived from bulk f(RH) (< 5 µm) (Eqs. 4 and 5) as well as from kappa derived from submicrometer AMS and SP2 species (Eq. 3) from the aircraft observations.

The CAM-chem modeled surface kappa values (Fig. 12) in the CAMP^{2}Ex region of interest, during the time when the three cases discussed in 3.2.1 and 3.2.2 were sampled, are within the range of globally modeled surface kappa in clean

585   marine (0.9 – 1.0), continental (0.1 – 0.4), and continental outflow / polluted marine (0.4 – 0.6) regions from previous

586   studies (Pringle et al., 2010). The highest modeled kappa (~1.0, Figs. 12a and 12b) is like those previously found in

587   clean marine areas. The high kappa values are influenced by the strong winds, which can increase sea salt emissions,

588   due to the tropical cyclone which was still developing on 16 September 2019 and more fully developed on 20

589   September 2019. The Pacific Ocean also is the source of high kappa (~0.9 - 1.0) for the shallow convection case on

590   24 September 2019 (Fig. 12c). For all three cases there was low kappa (< 0.4) in areas with low wind speeds and over

591   land especially over Borneo and East Asia, typical of continental and continental outflow regions. For the two cases

592   that were within the southwest monsoon (Figs. 13a and 13b) the lowest kappa values (< 0.2) were in Borneo and

593   downwind areas including Southern Philippines and areas east of it.

594   The modeled surface kappa (~0.1 – 0.5) below the aircraft positions for the case studies of interest (pink lines in Fig.

595   12), though over the sea, are lower than in those areas most affected by the Pacific Ocean and are influenced by

596   emissions from Borneo (Figs. 7a and 12a), East Asia (Figs. 9a and 12b) and the Philippines (Fig. 9c and 12c) based

597   on back trajectories. Kappa, calculated from the median f(RH) derived from scattering measurements, for the five air

598   masses discussed in sections 3.1 and 3.2 (MC: -0.02, EA: 0.14, PSEA: 0.10, WP: 0.24, and Other: 0.11), all fall in the

599   continental category even though the majority of these air masses are technically in regions with continental outflow

600   or polluted marine regions. The CAM-chem kappa values for the aircraft positions for the case studies with vertical

601   transport (Figs. 12b and 12c) the CAM-chem kappa values (~0.40 – 0.50) are more than double the range of calculated

602   kappa from East Asia (0.14) and Other (0.11) air masses that are influencing the case studies. To make sense of this

603   difference between globally modeled surface kappa values and that which is calculated from the CAMP^{2}Ex f(RH), we

604   delve more into aerosol vertical transport and its connection to aerosol hygroscopicity and evaluate the vertical profile

605   of the kappa calculated from the CAM-chem model outputs.
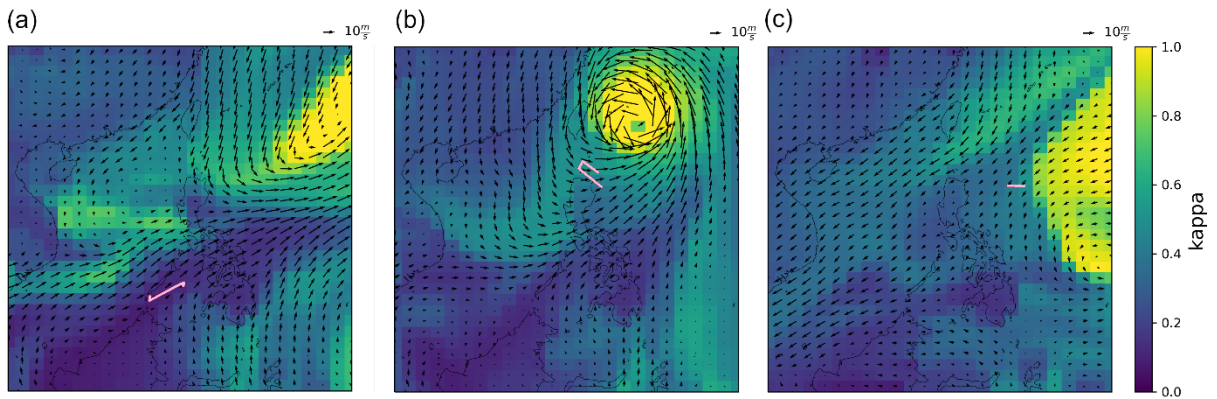
607   **Fig. 12. Modeled kappa and winds at 957 hPa for (a) the biomass burning smoke case at 06:00 UTC on 16 September 2019,**
608   **(b) the tropical cyclone-induced case at 06:00 UTC on 20 September 2019 and, (c) the shallow convection case at 06:00 UTC**
609   **on 24 September 2019. The pink lines represent the aircraft locations from 02:15 to 04:22 UTC on 16 September 2019, 01:53**
610   **to 06:20 UTC on 20 September 2019 and, from 02:55 to 06:02 UTC on 24 September 2019. The approximate aircraft**
611   **locations are represented by pink lines.**

612   The CAM-chem model (Fig. 13a) was able to represent the general trends in the observed total submicrometer mass
613   vertical profile for the tropical cyclone-induced convection case. The observations from AMS are only for non-
614   refractory aerosol species, however, and so sea salt and dust are not included in the total mass, possibly affecting the
615   comparison with the model output, which accounts for both. The uniform ~111 km grid mesh CAM-chem and
616   MUSICA outputs show approximate contributions by sea salt and dust to be 5 to 20% of the total mass (Figs. 13d and
617   13e). This could explain the higher total mass values from the model outputs compared to observations for some
618   altitude levels, though in general even without dust and sea salt the CAM-chem model still has slightly higher aerosol
619   total mass values (dashed lines in Fig. 13a) compared to the observations. The CAM-chem model represents the
620   approximate aerosol total mass well for this case probably because of its large-scale nature, where wind speeds were
621   high (> 20 m s^{-1}) and where the aerosol particles are potentially from a large source (East Asia) (Figs. 9a and 13a).
622   Together, the sum of the sulfate and ammonium mass fractions are similar for the observed (Fig. 13c) and modeled
623   outputs close to the surface (Figs. 13d and 13e), where the model output is ammonium bisulfate and not just sulfate,
624   but the actual mass concentrations of sulfate from the models are generally higher than the observations above 1 km
625   (Fig. S1a). This sulfate-based compound dominates the total aerosol mass for both the observations and model outputs,
626   as is expected based on its source air mass from East Asia, and accounts for the similar observed and modeled total
627   mass shape profiles (Fig. S1). The organic mass fraction, on the other hand, is lower by almost half of the observed
628   organic mass fraction due to sulfate dominating. This has a direct effect on modeled aerosol hygroscopicity (kappa),
629   as it was shown earlier that f(RH) decreases with an increased organic mass fraction (Fig. 4).

630
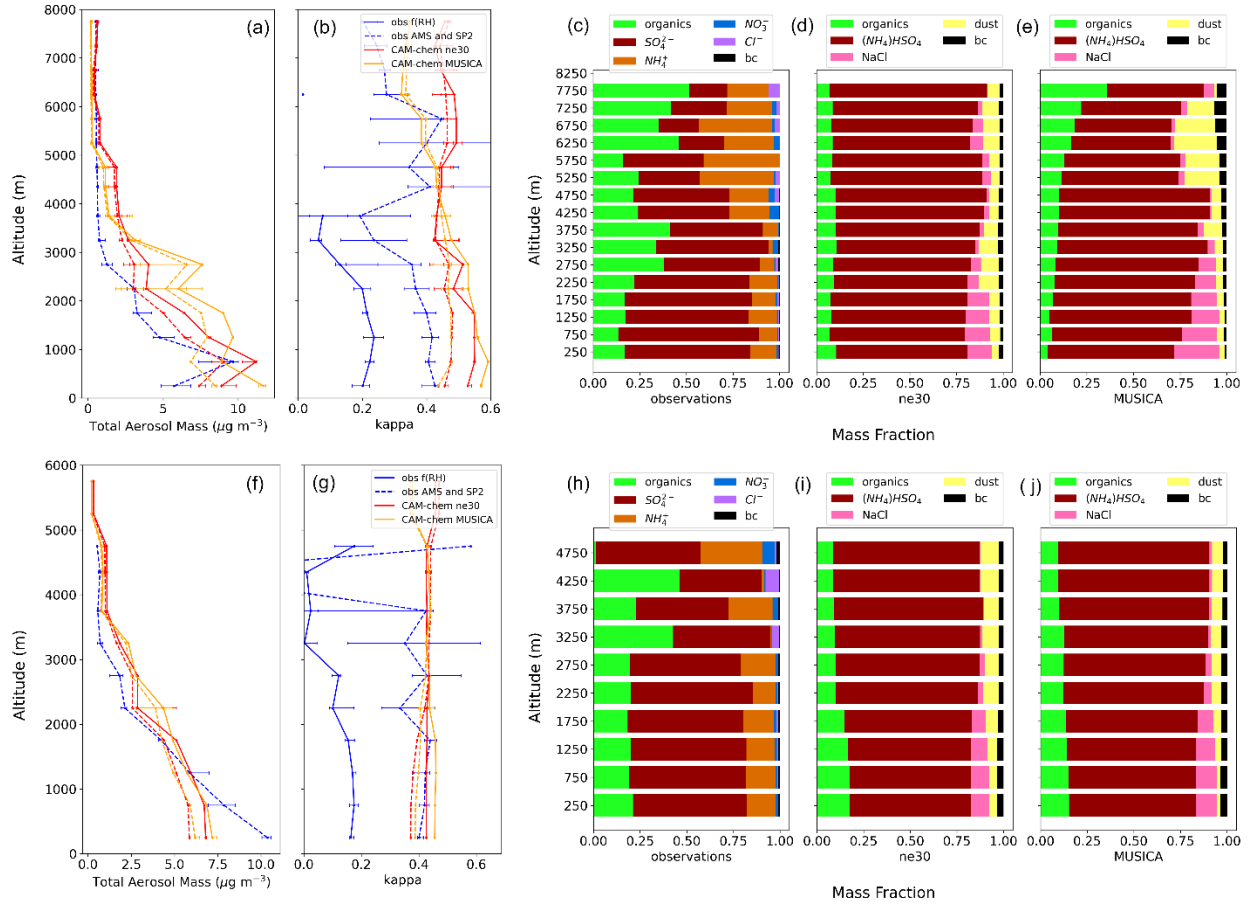
Figure 13. Vertical profiles of observed data and CAM-chem model outputs for ne30 ~1° and MUSICA 0.25° grids for (a-e) the tropical cyclone-induced convection case on 20 September 2019 and (f-j) the shallow convection case on 24 September 2019 at 500 m intervals. (a) Total observed submicrometer aerosol mass (01:53 to 06:20 UTC) from AMS (organics, SO$_4^{2-}$, NO$_3^-$, NH$_4^+$, Cl$^-$) and SP2 (black carbon (BC)) data and CAM-chem output (06:00 UTC) (organics: primary/hydrophobic, hygroscopic, and secondary (C$_{15}$H$_{38}$O$_2$), sulfate (NH$_4$HSO$_4$), sea salt, dust (AlSiO$_5$), and black carbon (primary/hydrophobic and hygroscopic)) where the solid line includes all the CAM-chem species and the dashed line excludes dust and sea salt and (b) calculated kappa from observed f(RH) (solid line, < 5 μm) and from AMS and SP2 (dashed line, submicrometer) data and using ZSR mixing rule for all CAM-chem aerosol species (solid line, submicrometer) and excluding dust and sea salt (dashed line). The lines correspond to the median values of data in the given altitude intervals and the bars correspond to the 25th and 75th percentile values. Submicrometer median mass fractions at 500 m intervals of (c) observational data (01:53 to 06:20 UTC) and (d-e) corresponding CAM-chem model outputs (06:00 UTC) for (d) ne30 ~1° and (e) MUSICA 0.25° grids for the tropical cyclone-induced convection case on 20 September 2019. CAM-chem outputs were combined into five main categories: organics (primary/hydrophobic, hygroscopic, and secondary (C$_{15}$H$_{38}$O$_2$)); sulfate (NH$_4$HSO$_4$); sea salt; dust (AlSiO$_5$); and black carbon (primary/hydrophobic and hygroscopic). (f) Total observed submicrometer aerosol mass (02:55 to 06:02 UTC) from AMS and SP2 data and (06:00 UTC) CAM-chem output and (g) calculated kappa from observed f(RH) and from AMS and SP2 data. Submicrometer median mass fractions of (h) observational data (02:55 to 06:02 UTC) and (i-j) corresponding CAM-chem model outputs (06:00 UTC) for the shallow convection case on 24 September 2019.

Median modeled kappa for the tropical cyclone-induced convection case is more than twice in magnitude compared to the median derived kappa from f(RH) (Fig. 13b), though they have a similar vertical profile shape. It has been noted

653   from previous studies that the conversion of observed f(RH) to kappa (Brock et al., 2016b) may be associated with up

654   to 40% uncertainty (van Diedenhoven et al., 2022), though this does not change that the kappa from CAM-chem is

655   still approximately twice the calculated observed kappa. We note that additional uncertainties as a result of the

656   conversion from Brock et al. (2016b) could also be contributing to the discrepancy. Brock et al. (2016b) used

657   submicrometer measurements in the southeast U.S. while CAMP[2]Ex f(RH) was calculated for particles less than 5

658   µm. Kappa calculated from f(RH) represents larger particles (< 5 µm) compared to the kappa calculated from CAM-

659   chem (< 0.48 µm), and the difference in size of the particles could be contributing to this disparity in kappa.

660   We compare more similar sized particles, kappa derived from AMS and SP2 measurements (< 0.70 µm) with kappa

661   calculated from CAM-chem (Fig. 13b), and find that the kappa derived from the AMS and SP2 is still lower than that

662   computed from CAM-chem outputs. The kappa from AMS and SP2 is approximately twice (100% larger than) the

663   kappa from f(RH), probably due to more than just particle size differences. Based on Mie theory and studies comparing

664   f(RH) of PM_1 and PM_{10} particles (Zieger et al., 2013; Titos et al., 2021), CAMP[2]Ex f(RH) would be larger if it were

665   measuring just submicrometer particles due to the increased scattering efficiency for accumulation mode particles

666   compared to coarse particles. Though, based on Fig. 3 of Titos et al. (2021), the difference in f(RH) in marine sites

667   would only be ~0.1 (given median observed SAE) and that would translate to ~20 to 40% increase in kappa. Thus,

668   although size plays a role, composition is also contributing to the difference in the calculated kappa values between

669   observations and the model. Examples of past studies in the region with low kappa values suggest that both the size

670   and compositional effect together are important. Lab experiments of tropical peat burning showed that smaller (70

671   nm) primary organic particles (POA) became more oxidized faster compared to larger particles (150 nm) and kappa

672   for oxidized POA (100 nm) was 0.16 (Chen et al., 2022). Ground measurements of aerosol particles (56 nm – 100 nm)

673   in Quezon City in the Philippines, which were dominated by elemental carbon, yielded kappa values less than 0.10

674   (AzadiAghdam et al., 2019).

675   The over and under-represented mass of sulfates and organics, respectively (Fig. 13b), by the model may be causing

676   the higher kappa in the model. Based on the discussion in section 3.1.2 on air masses coming from East Asia (Fig.

677   4c), as is the case for this event, an organic mass fraction that is lower by half can increase the f(RH) (f(RH = (-0.81

678   * organic mass fraction) + 1.56) and therefore the derived kappa by ~70%. Organics, especially secondary organic

679   aerosols have been underpredicted by CAM-chem in urban and urban outflow regions (Schwantes et al., 2022). This

680   is consistent with the observations for this case, which is influenced by urban outflow from East Asia and thus affecting

681   the calculated kappa from the model. CO (Fig. S1) is also underrepresented by the model potentially due to emissions

682   inventories (Hua et al., 2024).

683   For the case of shallow convection, the shape of the vertical profile of the CAM-chem model output total mass

684   concentration is similar to the observed total mass concentration profile (Fig. 13f), though it underestimates the

685   observed total concentration by approximately 2 to 4.5 µg m^{-3} below 1 km altitude, and then overestimates

686   concentrations by approximately 0.5 to 2 µg m^{-3} above 1 km. This is due to the model underestimating organics and

687   sulfate close to the surface, while sulfate is overestimated above 1 km (Fig. S1b). The effect of this is seen in the

688   model-derived kappa, which is, like the previous case, higher than the calculated kappa from observations, though to
689   a lesser degree (Fig. 13g). Unlike the case of the tropical cyclone-induced convection, the modeled kappa is relatively
690   unchanging in shape compared to the kappa derived from observations. This is likely due to the differences in the
691   compositional profile at the higher altitudes, even if the total mass is similar. The model is not able to represent the
692   increase and decrease in organic mass fraction from 3.5 to 4.5 km (Fig. 13h) and dominance of sulfate above 4.5 km.
693   At those altitudes the observations become dominated by sulfate, ammonium, and nitrate (Fig. 13h), even with losses
694   due to scavenging and activation as shown by decreased aerosol mass with altitude, probably due to the in-cloud
695   production of sulfate as discussed in section 3.2.2. The mass fraction profiles from the model (Figs. 13i and 13j) appear
696   to have a steadily decreasing (increasing) organic and sea salt (sulfate and dust) mass fraction with height. This case
697   is a smaller scale event with smaller surface winds associated with it (Fig. 12b) compared to the tropical cyclone case.
698   With weak forcing, it is likely that the CAM cumulus parameterizations does not predict the convection observed in
699   the shallow convection case affecting modeled aerosol mass vertical distribution and, consequently, kappa in both the
700   uniform ~111 global model and the regionally refined simulations. This is similar to a model evaluation study (i.e.
701   GEOS and GOCART) of CAMP^{2}Ex aerosol extinction data, which recommended an improvement of shallow
702   convection schemes to improve the representation of vertical transport (Collow et al., 2022). In fact, the CO increase
703   above 5 km, that that we used to identify convection, is not captured by CAM-chem (Fig. S2). What is consistent
704   though is that for both the observations and model output of this shallow convection case, the relative magnitude of
705   the model kappa is lower than that of the tropical cyclone case.

4. Conclusion

707   This study reports on low PM$_5$ (D$_p$ < 5 µm) aerosol hygroscopicity measured during CAMP^{2}Ex 2019 in Southeast
708   Asia due to organics from biomass burning. Aging and vertical transport changes the hygroscopicity of particles
709   affecting clouds in the region. Comparisons with a global atmospheric chemistry model reveal discrepancies between
710   observed and modeled aerosol concentrations and hygroscopicity, emphasizing the need to improve emissions
711   inventories and shallow cloud parameterizations. Notable results of this work, following the study goals raised at the
712   end of Section 1 are as follows:

713   The generally low median f(RH) (1.24 with Q1 and Q3 of 1.05 and 1.43, respectively) of aerosol particles (< 5 µm)
714   in Southeast Asia during the CAMP^{2}Ex campaign from 24 August to 5 October in 2019 is linked to the dominating
715   regional effect of biomass burning from the Maritime Continent. Measurements of f(RH) in other polluted marine
716   environments around the world for PM$_{10}$ (< 10 µm) and PM$_1$ (< 1 µm) particles have higher ranges (median of ~1.7 –
717   2.0) of f(RH) values (Titos et al., 2021). The median f(RH) of air masses from the Maritime Continent was
718   exceptionally low (1.05 with Q1 and Q3 of 0.94 and 1.20, respectively) for polluted marine environments and are
719   more similar to those with biomass burning (Gomez et al., 2018). The air masses with the highest f(RH) from
720   CAMP^{2}Ex are generally from the West Pacific, in the northernmost regions of the Philippines and farthest away from
721   the Maritime Continent. Their median f(RH) (1.49 with Q1 and Q3 of 1.26 and 1.73, respectively) is also lower than
722   what has been associated with typical polluted marine environments.

723 Throughout CAMP²Ex, submicrometer organic matter is the main aerosol component associated with biomass burning

724 and the low f(RH) values. Organics are a major feature of total aerosol mass, especially in air masses traced back to

725 the Maritime Continent. Biomass burning smoke is spread out in the region increasing AOD downwind of the MC

726 (Fig. 2 in Reid et al. (2023)) and is corroborated by cases of sub-1 f(RH) and submicrometer reflective particles with

727 elevated organic mass fractions that are present in all the air masses. Based on clustering analysis using optical

728 properties, majority of the particles sampled during the campaign appear to be a mixture of both organic and elemental

729 carbon. Organics dominate in terms of mass fraction due to the smoldering-type burning in peat fire (Reid et al., 2023)

730 from the Maritime Continent, which is known to produce more organics than elemental carbon (Reid et al., 2005).

731 This is consistent with what Miller et al. (2023) observed where the highest median levels of organic and elemental

732 carbon mass during CAMP²Ex were due to biomass burning from the Maritime Continent. Without organics, the

733 baseline f(RH) (1.38 – 1.55, Fig. 4), is still lower than measurements from other areas (i.e. 2.19 from SEAC⁴RS in

734 and around the U.S.) (Shingler et al., 2016a) probably due to the presence of elemental carbon, which is the second

735 most dominant aerosol type during the campaign.

736 Farther away from the Maritime Continent, the organic particles have aged and become more oxidized as they

737 interacted with the other air masses. The West Pacific is a remote region in northern Philippines and is downwind of

738 biomass burning from MC, resulting in a combined marine and polluted aerosol. The oldest biomass burning aerosols

739 were observed there. The organic oxidation values of the aerosol particles in the air mass from the West Pacific are

740 close to the threshold of maximum oxidation that has been observed in previous studies (Cubison et al., 2011). Vertical

741 transport decreases and increases hygroscopicity at cloud level with increased organic and sulfate mass fractions,

742 respectively, in the West Pacific. These aerosol constituents are thought to be transported from the MC and the

743 Philippines and their surrounding oceans, where natural and industrial sources are significant (Miller et al., 2023), and

744 then cloud processed.

745 Evaluation of the global chemical transport CAM-chem model at two output grids (~111 km and 25 km) against two

746 convective cases from CAMP²Ex show the underrepresentation of organics in general and a higher derived aerosol

747 hygroscopicity (kappa), which may be linked to the possible overestimation of aerosol hygroscopicity from biomass

748 burning based on studies of aerosol optical depth and extinction in the area (Collow et al., 2022; Edwards et al., 2022).

749 CAM-chem overestimates sulfate in the tropical cyclone induced convection case, consistent with results from an

750 assessment of the NAAPS reanalysis product on the positive bias of sulfate from East Asia (Edwards et al., 2022).

751 The vertical representation of the aerosol composition for the larger scale convection case due to a tropical cyclone is

752 better than that for the shallow convection case. Cloud processing and increased hygroscopicity are not captured by

753 the model for the shallow convection case, irrespective of model grid size. The representation of shallow convection

754 in the area by global models remains challenging, based on other model-evaluation studies (Collow et al., 2022). Past

755 studies on biomass burning aerosol effects on convection in Southeast Asia using a cloud-scale model emphasized the

756 importance of aerosol composition and absorptive properties, and their effect on atmospheric stability, in the

757 understanding of aerosol-cloud interactions (Hodzic and Duvel, 2018). It is thus ideal that cloud-scale models be

758 evaluated using the dataset from CAMP²Ex, where the invigoration of shallow clouds has been observed (Reid et al.,
759 2023).

760 The implications of the low aerosol hygroscopicity in the region and its effects on clouds and climate are just beginning
761 to be unraveled. The mixing and aging of organic and elemental carbon from biomass burning smoke in the Maritime
762 Continent with background and transported sources influences hygroscopicity observations and modeling
763 uncertainties and can be the topic of future work. Improvements in harmonization in terms of aerosol particle sizes
764 and composition, along with updated emissions inventories, will be helpful moving forward both for the observations
765 and modeling of aerosol hygroscopicity. These suggestions can hopefully improve shallow cumulus representation,
766 which is still the biggest source of differences in model sensitivity in the understanding of climate change (Bony and
767 Dufresne, 2005), in the region and globally. Emerging endeavors to implement higher resolution schemes in a large
768 domain (Pfister et al., 2020; Radtke et al., 2021) to capture both fine scale aerosol-cloud processes along with
769 improved observations in Southeast Asia hold promise.

770

771 *Data availability.* CAMP²Ex data can be found at https://doi.org/10.5067/Suborbital/CAMP2EX2018/DATA001.
772 CAM-chem model outputs can be found at https://doi.org/10.6084/m9.figshare.26755936.v1.

773

774 *Author contributions.* LDZ, ECC, JPDG, GSD, RF, MRAH, MS, JW, QX, and AS carried out various aspects of the
775 data collection. ST and JZ conducted the CAM-chem model simulations. GRL, LDZ, AFA, MB, ECC, RF, MRAH,
776 MS, JW, QX, and AS performed analysis and interpretation of the data. GRL and AS prepared the manuscript with
777 contributions from the coauthors.

778

779 *Competing interests.* At least one of the (co-)authors is a member of the editorial board of *Atmospheric Chemistry and*
780 *Physics.*

781

782 *Special issue statement.* This article is part of the special issue "Cloud Aerosol and Monsoon Processes Philippines
783 Experiment (CAMP²Ex) (ACP/AMT inter-journal SI)". It is not associated with a conference.

784

785 *Acknowledgements.* The authors gratefully acknowledge the NOAA Air Resources Laboratory (ARL) for the
786 provision of the HYSPLIT transport and dispersion model and READY website (https://www.ready.noaa.gov) used
787 in this publication. The NSF National Center for Atmospheric Research is a major facility sponsored by the U.S.
788 National Science Foundation under Cooperative Agreement No. 1852977.

789

790 *Financial support.* This research has been supported by the National Aeronautics and Space Administration (grant
791 no. 80NSSC18K0148) and ONR grant N00014-21-1-2115.

792

References

Adam, M. G., Tran, P. T., Bolan, N., and Balasubramanian, R.: Biomass burning-derived airborne particulate matter in Southeast Asia: A critical review, Journal of Hazardous Materials, 407, 124760, https://doi.org/10.1016/j.jhazmat.2020.124760, 2021.

Amnuaylojaroen, T.: Air Pollution Modeling in Southeast Asia—An Overview, Vegetation Fires and Pollution in Asia, 531-544, https://doi.org/10.1007/978-3-031-29916-2_31, 2023.

Anderson, T. L., and Ogren, J. A.: Determining aerosol radiative properties using the TSI 3563 integrating nephelometer, Aerosol Science and Technology, 29, 57-69, https://doi.org/10.1080/02786829808965551, 1998.

Ångström, A.: On the atmospheric transmission of sun radiation and on dust in the air, Geografiska Annaler, 11, 156-166, https://doi.org/10.1080/20014422.1929.11880498, 1929.

Attwood, A., Washenfelder, R., Brock, C., Hu, W., Baumann, K., Campuzano-Jost, P., Day, D., Edgerton, E., Murphy, D., and Palm, B.: Trends in sulfate and organic aerosol mass in the Southeast US: Impact on aerosol optical depth and radiative forcing, Geophysical Research Letters, 41, 7701-7709, https://doi.org/10.1002/2014GL061669, 2014.

AzadiAghdam, M., Braun, R. A., Edwards, E.-L., Bañaga, P. A., Cruz, M. T., Betito, G., Cambaliza, M. O., Dadashazar, H., Lorenzo, G. R., and Ma, L.: On the nature of sea salt aerosol at a coastal megacity: Insights from Manila, Philippines in Southeast Asia, Atmos. Environ., 216, 116922, https://doi.org/10.1016/j.atmosenv.2019.116922, 2019.

Barth, M., Rasch, P., Kiehl, J., Benkovitz, C., and Schwartz, S.: Sulfur chemistry in the National Center for Atmospheric Research Community Climate Model: Description, evaluation, features, and sensitivity to aqueous chemistry, J. Geophys. Res.- Atmos., 105, 1387-1415, https://doi.org/10.1029/1999JD900773, 2000.

Baynard, T., Garland, R., Ravishankara, A., Tolbert, M., and Lovejoy, E.: Key factors influencing the relative humidity dependence of aerosol light scattering, Geophysical research letters, 33, https://doi.org/10.1029/2005GL024898, 2006.

Bergstrom, R. W., Pilewskie, P., Russell, P. B., Redemann, J., Bond, T. C., Quinn, P. K., and Sierau, B.: Spectral absorption properties of atmospheric aerosols, Atmos. Chem. Phys., 7, 5937-5943, https://doi.org/10.5194/acp-7-5937-2007, 2007.

Bony, S., and Dufresne, J. L.: Marine boundary layer clouds at the heart of tropical cloud feedback uncertainties in climate models, Geophysical Research Letters, 32, https://doi.org/10.1029/2005GL023851, 2005.

Brock, C., Wagner, N., and Gordon, T.: Effect of Aerosol Size and Hygroscopicity on Aerosol Optical Depth in the Southeastern United States, EGU General Assembly Conference Abstracts, 2016a.

Brock, C. A., Wagner, N. L., Anderson, B. E., Attwood, A. R., Beyersdorf, A., Campuzano-Jost, P., Carlton, A. G., Day, D. A., Diskin, G. S., and Gordon, T. D.: Aerosol optical properties in the southeastern United States in summer-Part 1: Hygroscopic growth, https://doi.org/10.5194/acp-16-4987-2016, 2016b.

Brooks, S. D., Wise, M. E., Cushing, M., and Tolbert, M. A.: Deliquescence behavior of organic/ammonium sulfate aerosol, Geophysical Research Letters, 29, 23-21-23-24, https://doi.org/10.1029/2002GL014733, 2002.

Burgos, M. A., Andrews, E., Titos, G., Alados-Arboledas, L., Baltensperger, U., Day, D., Jefferson, A., Kalivitis, N., Mihalopoulos, N., and Sherman, J.: A global view on the effect of

water uptake on aerosol particle light scattering, Scientific data, 6, 1-19, https://doi.org/10.1038/s41597-019-0158-7, 2019.

Cazorla, A., Bahadur, R., Suski, K., Cahill, J. F., Chand, D., Schmid, B., Ramanathan, V., and Prather, K.: Relating aerosol absorption due to soot, organic carbon, and dust to emission sources determined from in-situ chemical measurements, Atmospheric Chemistry and Physics, 13, 9337-9350, https://doi.org/10.5194/acp-13-9337-2013, 2013.

Chandra, A. S., Zhang, C., Klein, S. A., and Ma, H. Y.: Low-cloud characteristics over the tropical western Pacific from ARM observations and CAM5 simulations, Journal of Geophysical Research: Atmospheres, 120, 8953-8970, https://doi.org/10.1002/2015JD023369, 2015.

Che, H., Segal-Rozenhaimer, M., Zhang, L., Dang, C., Zuidema, P., Dobracki, A., Sedlacek III, A. J., Coe, H., Wu, H., and Taylor, J.: Cloud processing and weeklong ageing affect biomass burning aerosol properties over the south-eastern Atlantic, Communications earth & environment, 3, 182, https://doi.org/10.1038/s43247-022-00517-3, 2022.

Chen, J., Zhao, C., Ma, N., and Yan, P.: Aerosol hygroscopicity parameter derived from the light scattering enhancement factor measurements in the North China Plain, Atmospheric Chemistry and Physics, 14, 8105-8118, https://doi.org/10.5194/acp-14-8105-2014, 2014.

Chen, J., Budisulistiorini, S. H., Itoh, M., and Kuwata, M.: Roles of relative humidity and particle size on chemical aging of tropical peatland burning particles: Potential influence of phase state and implications for hygroscopic property, Journal of Geophysical Research: Atmospheres, 127, e2022JD036871, https://doi.org/10.5194/acp-22-13219-2022, 2022.

Chen, Q., McGowan, S., Gouramanis, C., Fong, L., Balasubramanian, R., and Taylor, D.: Rapidly rising transboundary atmospheric pollution from industrial and urban sources in Southeast Asia and its implications for regional sustainable development, Environ. Res. Lett., 15, 1040a1045, https://doi.org/10.1088/1748-9326/abb5ce, 2020.

Collow, A. B. M., Buchard, V., Colarco, P. R., da Silva, A. M., Govindaraju, R., Nowottnick, E. P., Burton, S., Ferrare, R., Hostetler, C., and Ziemba, L.: An evaluation of biomass burning aerosol mass, extinction, and size distribution in GEOS using observations from CAMP 2 Ex, Atmospheric Chemistry and Physics, 22, 16091-16109, https://doi.org/10.5194/acp-22-16091-2022, 2022.

Covert, D. S., Charlson, R., and Ahlquist, N.: A study of the relationship of chemical composition and humidity to light scattering by aerosols, Journal of Applied Meteorology, 11, 968-976, https://doi.org/10.1175/1520-0450(1972)011<0968:ASOTRO>2.0.CO;2, 1972.

Crosbie, E., Ziemba, L. D., Shook, M. A., Robinson, C. E., Winstead, E. L., Thornhill, K. L., Braun, R. A., MacDonald, A. B., Stahl, C., and Sorooshian, A.: Measurement report: Closure analysis of aerosol–cloud composition in tropical maritime warm convection, Atmos. Chem. Phys., 22, 13269-13302, https://doi.org/10.5194/acp-22-13269-2022, 2022.

Crumeyrolle, S., Gomes, L., Tulet, P., Matsuki, A., Schwarzenboeck, A., and Crahan, K.: Increase of the aerosol hygroscopicity by cloud processing in a mesoscale convective system: a case study from the AMMA campaign, Atmospheric Chemistry and Physics, 8, 6907-6924, https://doi.org/10.5194/acp-8-6907-2008, 2008.

Cruz, M. T., Bañaga, P. A., Betito, G., Braun, R. A., Stahl, C., Aghdam, M. A., Cambaliza, M. O., Dadashazar, H., Hilario, M. R., Lorenzo, G. R., Ma, L., MacDonald, A. B., Pabroa, C., Yee, J. R., Simpas, J. B., and Sorooshian, A.: Size-resolved composition and morphology of particulate matter during the southwest monsoon in Metro Manila, Philippines, Atmos. Chem. Phys., 19, 10675–10696, https://doi.org/10.5194/acp-19-10675-2019, 2019.

882 Cubison, M., Ortega, A., Hayes, P., Farmer, D., Day, D., Lechner, M., Brune, W., Apel, E.,
883 Diskin, G., and Fisher, J.: Effects of aging on organic aerosol from open biomass burning smoke
884 in aircraft and laboratory studies, Atmospheric Chemistry and Physics, 11, 12049-12064,
885 https://doi.org/10.5194/acp-11-12049-2011, 2011.
886 Dadashazar, H., Corral, A. F., Crosbie, E., Dmitrovic, S., Kirschler, S., McCauley, K., Moore,
887 R., Robinson, C., Schlosser, J. S., and Shook, M.: Organic enrichment in droplet residual
888 particles relative to out of cloud over the northwestern Atlantic: analysis of airborne ACTIVATE
889 data, Atmospheric Chemistry and Physics, 22, 13897-13913, https://doi.org/10.5194/acp-22-
890 13897-2022, 2022.
891 Dockery, D. W.: Epidemiologic evidence of cardiovascular effects of particulate air pollution,
892 Environmental health perspectives, 109, 483-486, https://doi.org/10.1289/ehp.01109s4483, 2001.
893 Dong, X., Fu, J. S., Huang, K., Lin, N.-H., Wang, S.-H., and Yang, C.-E.: Analysis of the co-
894 existence of long-range transport biomass burning and dust in the subtropical West Pacific
895 Region, Scientific Reports, 8, 8962, https://doi.org/10.1038/s41598-018-27129-2, 2018.
896 Dubovik, O., Holben, B., Eck, T. F., Smirnov, A., Kaufman, Y. J., King, M. D., Tanré, D., and
897 Slutsker, I.: Variability of absorption and optical properties of key aerosol types observed in
898 worldwide locations, J. Atmos. Sci., 59, 590-608, https://doi.org/10.1175/1520-
899 0469(2002)059<0590:VOAAOP>2.0.CO;2, 2002.
900 Duplissy, J., DeCarlo, P. F., Dommen, J., Alfarra, M. R., Metzger, A., Barmpadimos, I., Prevot,
901 A. S., Weingartner, E., Tritscher, T., and Gysel, M.: Relating hygroscopicity and composition of
902 organic aerosol particulate matter, Atmospheric Chemistry and Physics, 11, 1155-1165,
903 https://doi.org/10.5194/acp-11-1155-2011, 2011.
904 Eck, T. F., Holben, B. N., Reid, J., Giles, D., Rivas, M., Singh, R. P., Tripathi, S., Bruegge, C.,
905 Platnick, S., and Arnold, G.: Fog-and cloud-induced aerosol modification observed by the
906 Aerosol Robotic Network (AERONET), J. Geophys. Res.- Atmos., 117,
907 https://doi.org/10.1029/2011JD016839, 2012.
908 Edwards, E.-L., Reid, J. S., Xian, P., Burton, S. P., Cook, A. L., Crosbie, E. C., Fenn, M. A.,
909 Ferrare, R. A., Freeman, S. W., and Hair, J. W.: Assessment of NAAPS-RA performance in
910 Maritime Southeast Asia during CAMP 2 Ex, Atmospheric Chemistry and Physics, 22, 12961-
911 12983, https://doi.org/10.5194/acp-22-12961-2022, 2022.
912 Engelhart, G., Asa-Awuku, A., Nenes, A., and Pandis, S.: CCN activity and droplet growth
913 kinetics of fresh and aged monoterpene secondary organic aerosol, Atmospheric Chemistry and
914 Physics, 8, 3937-3949, https://doi.org/10.5194/acp-8-3937-2008, 2008.
915 Faloona, I.: Sulfur processing in the marine atmospheric boundary layer: A review and critical
916 assessment of modeling uncertainties, Atmos. Environ., 43, 2841-2854,
917 https://doi.org/10.1016/j.atmosenv.2009.02.043, 2009.
918 Fan, X., Liu, J., Zhang, F., Chen, L., Collins, D., Xu, W., Jin, X., Ren, J., Wang, Y., and Wu, H.:
919 Contrasting size-resolved hygroscopicity of fine particles derived by HTDMA and HR-ToF-
920 AMS measurements between summer and winter in Beijing: the impacts of aerosol aging and
921 local emissions, Atmospheric Chemistry and Physics, 20, 915-929, https://doi.org/10.5194/acp-
922 20-915-2020, 2020.
923 Ferrare, R., Melfi, S., Whiteman, D., Evans, K., Poellot, M., and Kaufman, Y.: Raman lidar
924 measurements of aerosol extinction and backscattering: 2. Derivation of aerosol real refractive
925 index, single-scattering albedo, and humidification factor using Raman lidar and aircraft size
926 distribution measurements, Journal of Geophysical Research: Atmospheres, 103, 19673-19689,
927 https://doi.org/10.1029/98JD01647, 1998.

Ferrare, R., Hair, J., Hostetler, C., Shingler, T., Burton, S. P., Fenn, M., Clayton, M., Scarino, A. J., Harper, D., and Seaman, S.: Airborne HSRL-2 measurements of elevated aerosol depolarization associated with non-spherical sea salt, Frontiers in Remote Sensing, 4, 1143944, https://doi.org/10.3389/frsen.2023.1143944, 2023.

Garland, R. M., Ravishankara, A., Lovejoy, E. R., Tolbert, M. A., and Baynard, T.: Parameterization for the relative humidity dependence of light extinction: Organic-ammonium sulfate aerosol, Journal of Geophysical Research: Atmospheres, 112, https://doi.org/10.1029/2006JD008179, 2007.

Garofalo, L. A., Pothier, M. A., Levin, E. J., Campos, T., Kreidenweis, S. M., and Farmer, D. K.: Emission and evolution of submicron organic aerosol in smoke from wildfires in the western United States, ACS Earth and Space Chemistry, 3, 1237-1247, https://doi.org/10.1021/acsearthspacechem.9b00125, 2019.

Gasparini, R., Collins, D. R., Andrews, E., Sheridan, P. J., Ogren, J. A., and Hudson, J. G.: Coupling aerosol size distributions and size-resolved hygroscopicity to predict humidity-dependent optical properties and cloud condensation nuclei spectra, Journal of Geophysical Research: Atmospheres, 111, https://doi.org/10.1029/2005JD006092, 2006.

Gomez, S. L., Carrico, C., Allen, C., Lam, J., Dabli, S., Sullivan, A., Aiken, A. C., Rahn, T., Romonosky, D., and Chylek, P.: Southwestern US biomass burning smoke hygroscopicity: The role of plant phenology, chemical composition, and combustion properties, Journal of Geophysical Research: Atmospheres, 123, 5416-5432, https://doi.org/10.1029/2017JD028162, 2018.

Hänel, G.: The properties of atmospheric aerosol particles as functions of the relative humidity at thermodynamic equilibrium with the surrounding moist air, in: Advances in geophysics, Elsevier, 73-188, 1976.

Hegg, D., Larson, T., and Yuen, P. F.: A theoretical study of the effect of relative humidity on light scattering by tropospheric aerosols, Journal of Geophysical Research: Atmospheres, 98, 18435-18439, https://doi.org/10.1029/93JD01928, 1993.

Hilario, M. R. A., Crosbie, E., Shook, M., Reid, J. S., Cambaliza, M. O. L., Simpas, J. B. B., Ziemba, L., DiGangi, J. P., Diskin, G. S., and Nguyen, P.: Measurement report: Long-range transport patterns into the tropical northwest Pacific during the CAMP 2 Ex aircraft campaign: chemical composition, size distributions, and the impact of convection, Atmos. Chem. Phys., 21, 3777-3802, https://doi.org/10.5194/acp-21-3777-2021, 2021.

Hilario, M. R. A., Barth, M., Bennett, R., Crosbie, E., DiGangi, J. P., Diskin, G. S., Lorenzo, G. R., Rutledge, S., Martin, M. Y., and Ziemba, L.: Quantifying scavenging efficiencies of different aerosol species and size-resolved volume concentrations in tropical convective clouds over the West Pacific, Journal of the Atmospheric Sciences, 82, 267-282, https://doi.org/10.1175/JAS-D-24-0064.1, 2025.

Hodzic, A., and Duvel, J. P.: Impact of biomass burning aerosols on the diurnal cycle of convective clouds and precipitation over a tropical island, Journal of Geophysical Research: Atmospheres, 123, 1017-1036, https://doi.org/10.1002/2017JD027521, 2018.

Hong, Y., and Di Girolamo, L.: Cloud phase characteristics over Southeast Asia from A-Train satellite observations, Atmos. Chem. Phys., 20, 8267-8291, https://doi.org/10.5194/acp-20-8267-2020, 2020.

Höpner, F., Bender, F. M., Ekman, A. M., Andersson, A., Gustafsson, Ö., and Leck, C.: Investigation of two optical methods for aerosol-type classification extended to a Northern

973   Indian Ocean site, Journal of Geophysical Research: Atmospheres, 124, 8743-8763,
974   https://doi.org/10.1029/2018JD029685, 2019.
975   Hua, W., Lou, S., Huang, X., Xue, L., Ding, K., Wang, Z., and Ding, A.: Diagnosing
976   uncertainties in global biomass burning emission inventories and their impact on modeled air
977   pollutants, Atmospheric Chemistry and Physics, 24, 6787-6807, https://doi.org/10.5194/acp-24-
978   6787-2024, 2024.
979   Kalberer, M.: Aerosol physics and chemistry, Encyclopedia of Atmospheric Sciences, 1, 23,
980   2014.
981   Kar, J., Bremer, H., Drummond, J. R., Rochon, Y. J., Jones, D. B., Nichitiu, F., Zou, J., Liu, J.,
982   Gille, J. C., and Edwards, D. P.: Evidence of vertical transport of carbon monoxide from
983   Measurements of Pollution in the Troposphere (MOPITT), Geophysical research letters, 31,
984   2004.
985   Kavouras, I. G., Nikolich, G., Etyemezian, V., DuBois, D. W., King, J., and Shafer, D.: In situ
986   observations of soil minerals and organic matter in the early phases of prescribed fires, Journal of
987   Geophysical Research: Atmospheres, 117, https://doi.org/10.1029/2011JD017420, 2012.
988   Köhler, H.: The nucleus in and the growth of hygroscopic droplets, Transactions of the Faraday
989   Society, 32, 1152-1161, 1936.
990   Kreidenweis, S., and Asa-Awuku, A.: Aerosol Hygroscopicity: Particle water content and its role
991   in atmospheric processes, https://doi.org/10.1016/B978-0-08-095975-7.00418-6, 2014.
992   Kuang, Y., Zhao, C., Tao, J., Bian, Y., Ma, N., and Zhao, G.: A novel method for deriving the
993   aerosol hygroscopicity parameter based only on measurements from a humidified nephelometer
994   system, Atmospheric Chemistry and Physics, 17, 6651-6662, https://doi.org/10.5194/acp-17-
995   6651-2017, 2017.
996   Kuang, Y., He, Y., Xu, W., Zhao, P., Cheng, Y., Zhao, G., Tao, J., Ma, N., Su, H., and Zhang,
997   Y.: Distinct diurnal variation in organic aerosol hygroscopicity and its relationship with
998   oxygenated organic aerosol, Atmospheric Chemistry and Physics, 20, 865-880, 2020.
999   Lacagnina, C., Hasekamp, O. P., Bian, H., Curci, G., Myhre, G., van Noije, T., Schulz, M.,
1000   Skeie, R. B., Takemura, T., and Zhang, K.: Aerosol single-scattering albedo over the global
1001   oceans: Comparing PARASOL retrievals with AERONET, OMI, and AeroCom models
1002   estimates, Journal of Geophysical Research: Atmospheres, 120, 9814-9836,
1003   https://doi.org/10.1002/2015JD023501, 2015.
1004   Lee, H.-H., Iraqui, O., Gu, Y., Yim, S. H.-L., Chulakadabba, A., Tonks, A. Y.-M., Yang, Z., and
1005   Wang, C.: Impacts of air pollutants from fire and non-fire emissions on the regional air quality in
1006   Southeast Asia, Atmos. Chem. Phys., 18, 6141-6156, https://doi.org/10.5194/acp-18-6141-2018,
1007   2018.
1008   Li, G., Bei, N., Cao, J., Huang, R., Wu, J., Feng, T., Wang, Y., Liu, S., Zhang, Q., and Tie, X.: A
1009   possible pathway for rapid growth of sulfate during haze days in China, Atmos. Chem. Phys., 17,
1010   3301-3316, https://doi.org/10.5194/acp-17-3301-2017, 2017.
1011   Liu, H., Zhao, C., Nekat, B., Ma, N., Wiedensohler, A., Van Pinxteren, D., Spindler, G., Müller,
1012   K., and Herrmann, H.: Aerosol hygroscopicity derived from size-segregated chemical
1013   composition and its parameterization in the North China Plain, Atmospheric Chemistry and
1014   Physics, 14, 2525-2539, https://doi.org/10.5194/acp-14-2525-2014, 2014.
1015   Liu, X., Ma, P.-L., Wang, H., Tilmes, S., Singh, B., Easter, R., Ghan, S., and Rasch, P.:
1016   Description and evaluation of a new four-mode version of the Modal Aerosol Module (MAM4)
1017   within version 5.3 of the Community Atmosphere Model, Geoscientific Model Development, 9,
1018   505-522, https://doi.org/10.5194/gmd-9-505-2016, 2016.

1019 Lorenzo, G. R., Arellano, A. F., Cambaliza, M. O., Castro, C., Cruz, M. T., Di Girolamo, L.,
1020 Gacal, G. F., Hilario, M. R. A., Lagrosas, N., Ong, H. J., Simpas, J. B., Uy, S. N., and
1021 Sorooshian, A.: An emerging aerosol climatology via remote sensing over Metro Manila, the
1022 Philippines, Atmospheric Chemistry and Physics, 23, 10579-10608, https://doi.org/10.5194/acp-
1023 23-10579-2023, 2023.
1024 Malm, W. C., and Day, D. E.: Estimates of aerosol species scattering characteristics as a function
1025 of relative humidity, Atmospheric Environment, 35, 2845-2860, https://doi.org/10.1016/S1352-
1026 2310(01)00077-2, 2001.
1027 Mason, B., Wagner, N., Adler, G., Andrews, E., Brock, C., Gordon, T., Lack, D., Perring, A.,
1028 Richardson, M., and Schwarz, J.: An intercomparison of aerosol absorption measurements
1029 conducted during the SEAC4RS campaign, Aerosol Science and Technology, 52, 1012-1027,
1030 https://doi.org/10.1080/02786826.2018.1500012, 2018.
1031 Maudlin, L., Wang, Z., Jonsson, H., and Sorooshian, A.: Impact of wildfires on size-resolved
1032 aerosol composition at a coastal California site, Atmospheric Environment, 119, 59-68,
1033 https://doi.org/10.1016/j.atmosenv.2015.08.039, 2015.
1034 McNaughton, C. S., Clarke, A. D., Howell, S. G., Pinkerton, M., Anderson, B., Thornhill, L.,
1035 Hudgins, C., Winstead, E., Dibb, J. E., and Scheuer, E.: Results from the DC-8 Inlet
1036 Characterization Experiment (DICE): Airborne versus surface sampling of mineral dust and sea
1037 salt aerosols, Aerosol Science and Technology, 41, 136-159,
1038 https://doi.org/10.1080/02786820601118406, 2007.
1039 Miller, R. M., Rauber, R. M., Di Girolamo, L., Rilloraza, M., Fu, D., McFarquhar, G. M.,
1040 Nesbitt, S. W., Ziemba, L. D., Woods, S., and Thornhill, K. L.: Influence of natural and
1041 anthropogenic aerosols on cloud base droplet size distributions in clouds over the South China
1042 Sea and West Pacific, Atmospheric Chemistry and Physics, 23, 8959-8977,
1043 https://doi.org/10.5194/acp-23-8959-2023, 2023.
1044 Mochida, M., Kuwata, M., Miyakawa, T., Takegawa, N., Kawamura, K., and Kondo, Y.:
1045 Relationship between hygroscopicity and cloud condensation nuclei activity for urban aerosols in
1046 Tokyo, Journal of Geophysical Research: Atmospheres, 111,
1047 https://doi.org/10.1029/2005JD006980, 2006.
1048 Moosmüller, H., and Sorensen, C.: Small and large particle limits of single scattering albedo for
1049 homogeneous, spherical particles, J. Quant. Spectrosc. Ra., 204, 250-255,
1050 https://doi.org/10.1016/j.jqsrt.2017.09.029, 2018.
1051 Nakajima, T., Higurashi, A., Takeuchi, N., and Herman, J. R.: Satellite and ground-based study
1052 of optical properties of 1997 Indonesian forest fire aerosols, Geophysical Research Letters, 26,
1053 2421-2424, https://doi.org/10.1029/1999GL900208, 1999.
1054 NASA, E. D.: Fires in Kalimantan, Indonesia, in, Worldview Image of the Week, 2020.
1055 Oanh, N. K., Upadhyay, N., Zhuang, Y.-H., Hao, Z.-P., Murthy, D., Lestari, P., Villarin, J.,
1056 Chengchua, K., Co, H., and Dung, N.: Particulate air pollution in six Asian cities: Spatial and
1057 temporal distributions, and associated sources, Atmospheric environment, 40, 3367-3380,
1058 https://doi.org/10.1016/j.atmosenv.2006.01.050, 2006.
1059 Othman, M., Latif, M. T., Hamid, H. H. A., Uning, R., Khumsaeng, T., Phairuang, W., Daud, Z.,
1060 Idris, J., Sofwan, N. M., and Lung, S.-C. C.: Spatial–temporal variability and health impact of
1061 particulate matter during a 2019–2020 biomass burning event in Southeast Asia, Scientific
1062 Reports, 12, 7630, https://doi.org/10.1038/s41598-022-11409-z, 2022.
1063 Palmer, T. Y.: Large fire winds, gases and smoke, Atmospheric Environment (1967), 15, 2079-
1064 2090, https://doi.org/10.1016/0004-6981(81)90241-9, 1981.

1065 Pawar, P. V., Ghude, S. D., Jena, C., Móring, A., Sutton, M. A., Kulkarni, S., Lal, D. M.,
1066 Surendran, D., Van Damme, M., and Clarisse, L.: Analysis of atmospheric ammonia over South
1067 and East Asia based on the MOZART-4 model and its comparison with satellite and surface
1068 observations, Atmospheric Chemistry and Physics, 21, 6389-6409, https://doi.org/10.5194/acp-
1069 21-6389-2021, 2021.
1070 Petters, M., and Kreidenweis, S.: A single parameter representation of hygroscopic growth and
1071 cloud condensation nucleus activity, Atmospheric Chemistry and Physics, 7, 1961-1971,
1072 https://doi.org/10.5194/acp-7-1961-2007, 2007.
1073 Pfister, G. G., Eastham, S. D., Arellano, A. F., Aumont, B., Barsanti, K. C., Barth, M. C.,
1074 Conley, A., Davis, N. A., Emmons, L. K., and Fast, J. D.: The multi-scale infrastructure for
1075 chemistry and aerosols (MUSICA), Bulletin of the American Meteorological Society, 101,
1076 E1743-E1760, https://doi.org/10.1175/BAMS-D-19-0331.1, 2020.
1077 Pokhrel, R. P., Gordon, J., Fiddler, M. N., and Bililign, S.: Impact of combustion conditions on
1078 physical and morphological properties of biomass burning aerosol, Aerosol Science and
1079 Technology, 55, 80-91, https://doi.org/10.1080/02786826.2020.1822512, 2021.
1080 Pringle, K., Tost, H., Pozzer, A., Pöschl, U., and Lelieveld, J.: Global distribution of the effective
1081 aerosol hygroscopicity parameter for CCN activation, Atmospheric Chemistry and Physics, 10,
1082 5241-5255, https://doi.org/10.5194/acp-10-5241-2010, 2010.
1083 Radtke, J., Mauritsen, T., and Hohenegger, C.: Shallow cumulus cloud feedback in large eddy
1084 simulations–bridging the gap to storm-resolving models, Atmospheric Chemistry and Physics,
1085 21, 3275-3288, https://doi.org/10.5194/acp-21-3275-2021, 2021.
1086 Reid, J., Koppmann, R., Eck, T., and Eleuterio, D.: A review of biomass burning emissions part
1087 II: intensive physical properties of biomass burning particles, Atmos. Chem. Phys., 5, 799-825,
1088 https://doi.org/10.5194/acp-5-799-2005, 2005.
1089 Reid, J., Maring, H., Narisma, G., van den Heever, S., Di Girolamo, L., Ferrare, R., Holz, R.,
1090 Lawson, P., Mace, G., and Simpas, J.: The coupling between tropical meteorology, aerosol
1091 lifecycle, convection, and radiation, during the Cloud, Aerosol and Monsoon Processes
1092 Philippines Experiment (CAMP 2 Ex), B. Am. Meteorol. Soc., https://doi.org/10.1175/BAMS-
1093 D-21-0285.1, 2023.
1094 Reid, J. S., Hyer, E. J., Johnson, R. S., Holben, B. N., Yokelson, R. J., Zhang, J., Campbell, J. R.,
1095 Christopher, S. A., Di Girolamo, L., and Giglio, L.: Observing and understanding the Southeast
1096 Asian aerosol system by remote sensing: An initial review and analysis for the Seven Southeast
1097 Asian Studies (7SEAS) program, Atmos. Res., 122, 403-468,
1098 https://doi.org/10.1016/j.atmosres.2012.06.005, 2013.
1099 Robinson, M. S., Chavez, J., Velazquez, S., and Jayanty, R.: Chemical speciation of PM2. 5
1100 collected during prescribed fires of the Coconino National Forest near Flagstaff, Arizona, Journal
1101 of the Air & Waste Management Association, 54, 1112-1123,
1102 https://doi.org/10.1080/10473289.2004.10470985, 2004.
1103 Rolph, G., Stein, A., and Stunder, B.: Real-time environmental applications and display system:
1104 READY, Environ. Modell. Softw., 95, 210-228, https://doi.org/10.1016/j.envsoft.2017.06.025,
1105 2017.
1106 Ross, A. D., Holz, R. E., Quinn, G., Reid, J. S., Xian, P., Turk, F. J., and Posselt, D. J.: Exploring
1107 the first aerosol indirect effect over Southeast Asia using a 10-year collocated MODIS, CALIOP,
1108 and model dataset, Atmospheric Chemistry and Physics, 18, 12747-12764,
1109 https://doi.org/10.5194/acp-18-12747-2018, 2018.

Saxena, P., Hildemann, L. M., McMurry, P. H., and Seinfeld, J. H.: Organics alter hygroscopic behavior of atmospheric particles, Journal of Geophysical Research: Atmospheres, 100, 18755-18770, https://doi.org/10.1029/95JD01835, 1995.

Schlosser, J. S., Braun, R. A., Bradley, T., Dadashazar, H., MacDonald, A. B., Aldhaif, A. A., Aghdam, M. A., Mardi, A. H., Xian, P., and Sorooshian, A.: Analysis of aerosol composition data for western United States wildfires between 2005 and 2015: Dust emissions, chloride depletion, and most enhanced aerosol constituents, J. Geophys. Res.- Atmos., 122, 8951-8966, https://doi.org/10.1002/2017JD026547, 2017.

Schuster, G. L., Dubovik, O., and Holben, B. N.: Angstrom exponent and bimodal aerosol size distributions, J. Geophys. Res.- Atmos., 111, https://doi.org/10.1029/2005JD006328, 2006.

Schwantes, R. H., Lacey, F. G., Tilmes, S., Emmons, L. K., Lauritzen, P. H., Walters, S., Callaghan, P., Zarzycki, C. M., Barth, M. C., and Jo, D. S.: Evaluating the impact of chemical complexity and horizontal resolution on tropospheric ozone over the conterminous US with a global variable resolution chemistry model, Journal of Advances in Modeling Earth Systems, 14, e2021MS002889, https://doi.org/10.1029/2021MS002889, 2022.

Shi, J., Hong, J., Ma, N., Luo, Q., He, Y., Xu, H., Tan, H., Wang, Q., Tao, J., and Zhou, Y.: Measurement report: On the difference in aerosol hygroscopicity between high and low relative humidity conditions in the North China Plain, Atmospheric Chemistry and Physics, 22, 4599-4613, https://doi.org/10.5194/acp-22-4599-2022, 2022.

Shingler, T., Crosbie, E., Ortega, A., Shiraiwa, M., Zuend, A., Beyersdorf, A., Ziemba, L., Anderson, B., Thornhill, L., and Perring, A. E.: Airborne characterization of subsaturated aerosol hygroscopicity and dry refractive index from the surface to 6.5 km during the SEAC4RS campaign, Journal of Geophysical Research: Atmospheres, 121, 4188-4210, https://doi.org/10.1002/2015JD024498, 2016a.

Shingler, T., Sorooshian, A., Ortega, A., Crosbie, E., Wonaschütz, A., Perring, A. E., Beyersdorf, A., Ziemba, L., Jimenez, J. L., and Campuzano-Jost, P.: Ambient observations of hygroscopic growth factor and f (RH) below 1: Case studies from surface and airborne measurements, Journal of Geophysical Research: Atmospheres, 121, 13,661-613,677, https://doi.org/10.1002/2016JD025471, 2016b.

Smith, S. J., Aardenne, J. v., Klimont, Z., Andres, R. J., Volke, A., and Delgado Arias, S.: Anthropogenic sulfur dioxide emissions: 1850–2005, Atmos. Chem. Phys., 11, 1101-1116, https://doi.org/10.5194/acp-11-1101-2011, 2011.

Sorooshian, A., Shingler, T., Crosbie, E., Barth, M., Homeyer, C., Campuzano-Jost, P., Day, D., Jimenez, J., Thornhill, K., and Ziemba, L.: Contrasting aerosol refractive index and hygroscopicity in the inflow and outflow of deep convective storms: Analysis of airborne data from DC3, Journal of Geophysical Research: Atmospheres, 122, 4565-4577, https://doi.org/10.1002/2017JD026638, 2017.

Spill, G., Stier, P., Field, P. R., and Dagan, G.: Effects of aerosol in simulations of realistic shallow cumulus cloud fields in a large domain, Atmospheric Chemistry and Physics, 19, 13507-13517, https://doi.org/10.5194/acp-19-13507-2019, 2019.

Stein, A., Draxler, R. R., Rolph, G. D., Stunder, B. J., Cohen, M., and Ngan, F.: NOAA's HYSPLIT atmospheric transport and dispersion modeling system, B. Am. Meteorol. Soc., 96, 2059-2077, https://doi.org/10.1175/BAMS-D-14-00110.1, 2015.

Stockwell, C. E., Jayarathne, T., Cochrane, M. A., Ryan, K. C., Putra, E. I., Saharjo, B. H., Nurhayati, A. D., Albar, I., Blake, D. R., and Simpson, I. J.: Field measurements of trace gases and aerosols emitted by peat fires in Central Kalimantan, Indonesia, during the 2015 El Niño,

Atmospheric Chemistry and Physics, 16, 11711-11732, https://doi.org/10.5194/acp-16-11711-2016, 2016.

Stokes, R., and Robinson, R.: Interactions in aqueous nonelectrolyte solutions. I. Solute-solvent equilibria, The Journal of Physical Chemistry, 70, 2126-2131, 1966.

Swietlicki, E., Hansson, H.-C., Hämeri, K., Svenningsson, B., Massling, A., McFiggans, G., McMurry, P. H., Petäjä, T., Tunved, P., and Gysel, M.: Hygroscopic properties of submicrometer atmospheric aerosol particles measured with H-TDMA instruments in various environments—a review, Tellus B: Chemical and Physical Meteorology, 60, 432-469, https://doi.org/10.1111/j.1600-0889.2008.00350.x, 2008.

Thalman, R., de Sá, S. S., Palm, B. B., Barbosa, H. M., Pöhlker, M. L., Alexander, M. L., Brito, J., Carbone, S., Castillo, P., and Day, D. A.: CCN activity and organic hygroscopicity of aerosols downwind of an urban region in central Amazonia: seasonal and diel variations and impact of anthropogenic emissions, Atmospheric Chemistry and Physics, 17, 11779-11801, https://doi.org/10.5194/acp-17-11779-2017, 2017.

Tilmes, S., Mills, M. J., Zhu, Y., Bardeen, C. G., Vitt, F., Yu, P., Fillmore, D., Liu, X., Toon, B., and Deshler, T.: Description and performance of a sectional aerosol microphysical model in the Community Earth System Model (CESM2), Geoscientific Model Development, 16, 6087-6125, https://doi.org/10.5194/gmd-16-6087-2023, 2023.

Titos, G., Burgos, M. A., Zieger, P., Alados-Arboledas, L., Baltensperger, U., Jefferson, A., Sherman, J., Weingartner, E., Henzing, B., and Luoma, K.: A global study of hygroscopicity-driven light-scattering enhancement in the context of other in situ aerosol optical properties, Atmospheric Chemistry and Physics, 21, 13031-13050, https://doi.org/10.5194/acp-21-13031-2021, 2021.

Tsay, S.-C., Hsu, N. C., Lau, W. K.-M., Li, C., Gabriel, P. M., Ji, Q., Holben, B. N., Welton, E. J., Nguyen, A. X., and Janjai, S.: From BASE-ASIA toward 7-SEAS: A satellite-surface perspective of boreal spring biomass-burning aerosols and clouds in Southeast Asia, Atmospheric environment, 78, 20-34, https://doi.org/10.1016/j.atmosenv.2012.12.013, 2013.

van Diedenhoven, B., Hasekamp, O. P., Cairns, B., Schuster, G. L., Stamnes, S., Shook, M., and Ziemba, L.: Remote sensing of aerosol water fraction, dry size distribution and soluble fraction using multi-angle, multi-spectral polarimetry, Atmospheric Measurement Techniques, 15, 7411-7434, https://doi.org/10.5194/amt-15-7411-2022, 2022.

Virkkula, A.: Correction of the calibration of the 3-wavelength Particle Soot Absorption Photometer (3λ PSAP), Aerosol Science and Technology, 44, 706-712, https://doi.org/10.1080/02786826.2010.482110, 2010.

Waggoner, A., Weiss, R., and Larson, T.: In-situ, rapid response measurement of H2SO4/(NH4)2SO4 aerosols in urban Houston: A comparison with rural Virginia, Atmospheric Environment (1967), 17, 1723-1731, https://doi.org/10.1016/0004-6981(83)90179-8, 1983.

Wang, X., Ye, X., Chen, H., Chen, J., Yang, X., and Gross, D. S.: Online hygroscopicity and chemical measurement of urban aerosol in Shanghai, China, Atmospheric Environment, 95, 318-326, https://doi.org/10.1016/j.atmosenv.2014.06.051, 2014.

Wang, Y., Li, Z., Zhang, Y., Du, W., Zhang, F., Tan, H., Xu, H., Fan, T., Jin, X., and Fan, X.: Characterization of aerosol hygroscopicity, mixing state, and CCN activity at a suburban site in the central North China Plain, Atmospheric Chemistry and Physics, 18, 11739-11752, https://doi.org/10.5194/acp-18-11739-2018, 2018.

Wu, Z., Zheng, J., Shang, D., Du, Z., Wu, Y., Zeng, L., Wiedensohler, A., and Hu, M.: Particle hygroscopicity and its link to chemical composition in the urban atmosphere of Beijing, China,

during summertime, Atmospheric Chemistry and Physics, 16, 1123-1138, https://doi.org/10.5194/acp-16-1123-2016, 2016.

Xu, W., Ovadnevaite, J., Fossum, K. N., Lin, C., Huang, R.-J., O'Dowd, C., and Ceburnis, D.: Aerosol hygroscopicity and its link to chemical composition in the coastal atmosphere of Mace Head: marine and continental air masses, Atmospheric Chemistry and Physics, 20, 3777-3791, https://doi.org/10.5194/acp-20-3777-2020, 2020.

Yang, Q., Easter, R. C., Campuzano-Jost, P., Jimenez, J. L., Fast, J. D., Ghan, S. J., Wang, H., Berg, L. K., Barth, M. C., and Liu, Y.: Aerosol transport and wet scavenging in deep convective clouds: A case study and model evaluation using a multiple passive tracer analysis approach, Journal of Geophysical Research: Atmospheres, 120, 8448-8468, https://doi.org/10.1002/2015JD023647, 2015.

Zhang, F., Wang, Y., Peng, J., Ren, J., Collins, D., Zhang, R., Sun, Y., Yang, X., and Li, Z.: Uncertainty in predicting CCN activity of aged and primary aerosols, Journal of Geophysical Research: Atmospheres, 122, 11,723-711,736, https://doi.org/10.1002/2017JD027058, 2017.

Zhao, G., Zhao, C., Kuang, Y., Bian, Y., Tao, J., Shen, C., and Yu, Y.: Calculating the aerosol asymmetry factor based on measurements from the humidified nephelometer system, Atmos. Chem. Phys., 18, 9049-9060, https://doi.org/10.5194/acp-18-9049-2018, 2018.

Zieger, P., Fierz-Schmidhauser, R., Weingartner, E., and Baltensperger, U.: Effects of relative humidity on aerosol light scattering: results from different European sites, Atmospheric Chemistry and Physics, 13, 10609-10631, https://doi.org/10.5194/acp-13-10609-2013, 2013.

Ziemba, L. D., Lee Thornhill, K., Ferrare, R., Barrick, J., Beyersdorf, A. J., Chen, G., Crumeyrolle, S. N., Hair, J., Hostetler, C., and Hudgins, C.: Airborne observations of aerosol extinction by in situ and remote-sensing techniques: Evaluation of particle hygroscopicity, Geophysical Research Letters, 40, 417-422, https://doi.org/10.1029/2012GL054428, 2013.